Synchronized Photoluminescence and Electrical Mobility Enhancement in 2D WS_2 through Sequence-Specific Chemical Passivation

Zhaojun Li[1,2,3]*, Ulrich Noumbe[2], Elin Berggren[2], Henry Nameirakpam[2], Takashi Kimura[4], Eito Asakura[4], Victor Gray[5], Tomas Edvinsson[1], Andreas Lindblad[2], Makoto Kohda[4], Rafael Araujo[1]*, Akshay Rao[3]*, M. Venkata Kamalakar[2]*

[1]Solid State Physics, Department of Materials Science and Engineering, Uppsala University, 75103 Uppsala, Sweden.

[2]X-ray Photon Science, Department of Physics and Astronomy, Uppsala University, 75120 Uppsala, Sweden.

[3]Cavendish Laboratory, University of Cambridge, JJ Thomson Avenue, CB3 0HE, Cambridge, United Kingdom

[4]Department of Materials Science, Tohoku University, Sendai 980-8579, Japan.

[5]Physical Chemistry, Department of Chemistry-Ångström Laboratory, Uppsala University, 75120 Uppsala, Sweden.

Email: zhaojun.li@angstrom.uu.se; rafael.araujo@angstrom.uu.se; ar525@cam.ac.uk; venkata.mutta@physics.uu.se

Abstract

Two-dimensional (2D) semiconducting dichalcogenides hold exceptional promise as optoelectronic materials for next-generation electronic and photonic devices, as well as their hybrid circuits. Despite this potential, the pervasive presence of defects in 2D dichalcogenides results in carrier mobility and photoluminescence (PL) that fall significantly short of theoretical predictions. Although defect passivation offers a potential solution, its effects have been inconsistent. This inconsistency arises from the current materials and methods, which fail to achieve the desired binding chemistry and band structure engineering necessary to enhance optical and electrical properties simultaneously. In this work, we uncover new binding chemistry using a sequence-specific chemical passivation (SSCP) protocol based on 2-furanmethanothiol (FSH) and bis(trifluoromethane) sulfonimide lithium salt (Li-TFSI), which allows us to demonstrate a synchronized 100-fold enhancement in both carrier mobility and photoluminescence (PL) in WS_2 monolayers. We propose a novel synergistic defect passivation mechanism, supported by ultrafast transient absorption spectroscopy (TA), Hard X-ray photoelectron spectroscopy (HAXPES), and density functional theory (DFT) calculations. Our

findings establish a new performance benchmark for the optical and electronic properties of WS_2 monolayers, paving the way for the development of more efficient and sustainable 2D semiconductor technologies.

Introduction

Atomically thin two-dimensional (2D) transition metal dichalcogenides (TMDs) have emerged as a new generation of semiconducting materials for electronic and optoelectronic applications.[1–5] Despite their extraordinary application potential, challenges persist in harnessing their full capabilities. 2D TMDs are predisposed to form atomic defects, such as chalcogenide vacancies, that cause charge carrier trapping in defect-induced potentials and result in non-radiative recombination pathways, thereby reducing charge carrier mobility.[6–8] Additionally, the strong electrostatic interactions in 2D TMDs enable the formation of trions, quasiparticles composed of an exciton and free charges, even at room temperature.[9–12] The existence of trions and defects strongly influence the intrinsic optical and electronic properties of TMDs. Despite extensive research focused on improving the semiconducting quality of 2D TMDs, the challenge remains in mitigating the defects within these materials.[13–20]

Photoluminescence (PL) intensity and charge carrier mobility (μ) are key indicators of the quality of 2D TMDs for optoelectronic applications, as they are sensitive to traps, structural defects, and charged impurities.[21–23] Among various approaches, surface chemical strategies stand out as versatile and non-destructive methods to enhance the properties of 2D TMDs.[16,24] In spite of advances in materials growth in recent years, our understating of defects, particularly the interaction of defects with passivating chemicals remains unclear.[25–27] Even the widely discussed treatment with organic super-acid H-TFSI results in trap-limited PL and potentially damages TMD materials and contacts, limiting its application in devices.[28,29] Although the benign chemical treatment based on Li-TFSI has led to a PL increase twice that of the H-TFSI, it does not lead to electrical mobility improvement.[30] Consequently, no chemical treatment has yet been able to significantly enhance both the PL and electrical mobility of 2D TMDs. Therefore, there is a pressing need for innovative chemical treatments that provide superior defect passivation, achieving synergetic enhancements of optical and electronic properties while ensuring compatibility with device fabrication.

In this work, by surface chemistry engineering of 2D WS_2 monolayers, we innovate a sequence-specific chemical passivation (SSCP) protocoL using 2-furanmethanothiol (FSH, the key

component of roasted coffee aroma) and bis(trifluoromethane) sulfonimide lithium salt (Li-TFSI). This chemical treatment protocol leads to 100-fold enhancements in both the charge carrier mobility and PL of mechanically exfoliated WS_2 monolayers on SiO_2 substrates, the highest enhancement factor observed with chemical passivation. The treatment also induces the largest blueshift in the PL peak position among all known surface treatments, signifying the most efficient p-doping effect and surpassing current benchmarks for the semiconducting quality of 2D WS_2. In addition, these non-corrosive chemicals are stable and operate in benign solvents under ambient conditions, making them sustainable and suitable for direct use during device fabrication of TMDs.

The ultrafast transient absorption spectroscopy (TA) and Hard X-ray photoelectron spectroscopy (HAXPES) demonstrate the high efficiency of the SSCP protocol without chemical modification of 2D WS_2. Supporting these experimental results, our density functional theory (DFT) calculations propose a novel atomic-level synergistic defect passivation mechanism. Our findings reveal that it is thermodynamically favorable for FSH molecules to be chemically adsorbed when two neighboring sulfur vacancies (SVs) are present. Additionally, the Li^+ ions are more stably adsorbed on the 2D WS_2 surface when coordinated by the FSH molecule, under both neutral and charged SV scenarios. This proposed mechanism opens new avenues for designing defect passivation chemicals for future electronic and optoelectronic applications.

Results and Discussion

Our SSCP protocol for 2D WS_2 monolayers (shown in Fig. S1) integrates a thiol-based small molecule, FSH, and an ionic salt, Li-TFSI. The chemical structures and the optimized procedures of this protocol are depicted in Fig. 1a. The FSH molecule consists of an electron-donating furan group which increases its acidity and facilitates its solubility in alcohol-based green solvents. The hydrophilic salt Li-TFSI also presents a high solubility in alcohol-based solvents. The WS_2 monolayer on a Si/SiO_2 substrate was obtained by gold-assisted mechanical exfoliation, which provides larger monolayers that enable extensive characterization techniques that require large-scale 2D materials. The WS_2 monolayer was immersed in a 0.01M FSH/Methanol solution for 6 hours. The extended duration ensures ample time for the FSH molecules to interact with the 2D WS_2 surface. Following this, the sample was subjected to a cleansing process, where it was immersed in a Methanol solvent for 48 hours. During this period, the solvent was replenished three times to ensure the removal of any excess FSH molecules that

had not strongly interacted with the 2D surface. Finally, the sample was immersed in a 0.02M Li-TFSI/Methanol solution for 40 minutes, after which it was air-dried without any additional washing steps. Notably, this stable chemical treatment protocol is developed in benign solvents and can be easily managed in an ambient atmosphere.

Following the SSCP protocol, the PL peak position exhibits a blueshift of over 30 meV throughout the entire monolayer flake, indicating that the macroscopic effect of this chemical treatment is p-doping (Fig. 1b).[30–32] Importantly, the PL of monolayer WS_2 is greatly enhanced, increasing by up to 200 times, as shown in Fig. 1c and d. The full width at half maximum (FWHM) of the treated PL spectra is also reduced to 26 meV, compared to 64 meV for the untreated sample. The PL spectra profile of the 2D WS_2 monolayer, measured immediately post-chemical treatment at room temperature, aligns with that measured at 4K in terms of the peak position and FWHM (Fig. 1e and Fig. S2). This alignment suggests a significant suppression of defects and trions in the 2D WS_2 following the SSCP.[33,34] Given the PL inhomogeneity of the monolayer WS_2 samples, we performed PL measurements on multiple WS_2 monolayer samples. A comprehensive discussion on the statistical distribution of the PL peak position and the enhancement factor of the PL intensity with varied chemical treatments (Fig. S3, S4) is available in Supplementary Information (SI) Note 4. The PL spectra of the treated sample underwent a redshift from 2.026 eV (612 nm) over time while stored in air, stabilizing at 2.019 eV (614 nm). This uniform change across the sample likely results from strain relaxation or doping from small molecules in the air.[19,35,36]

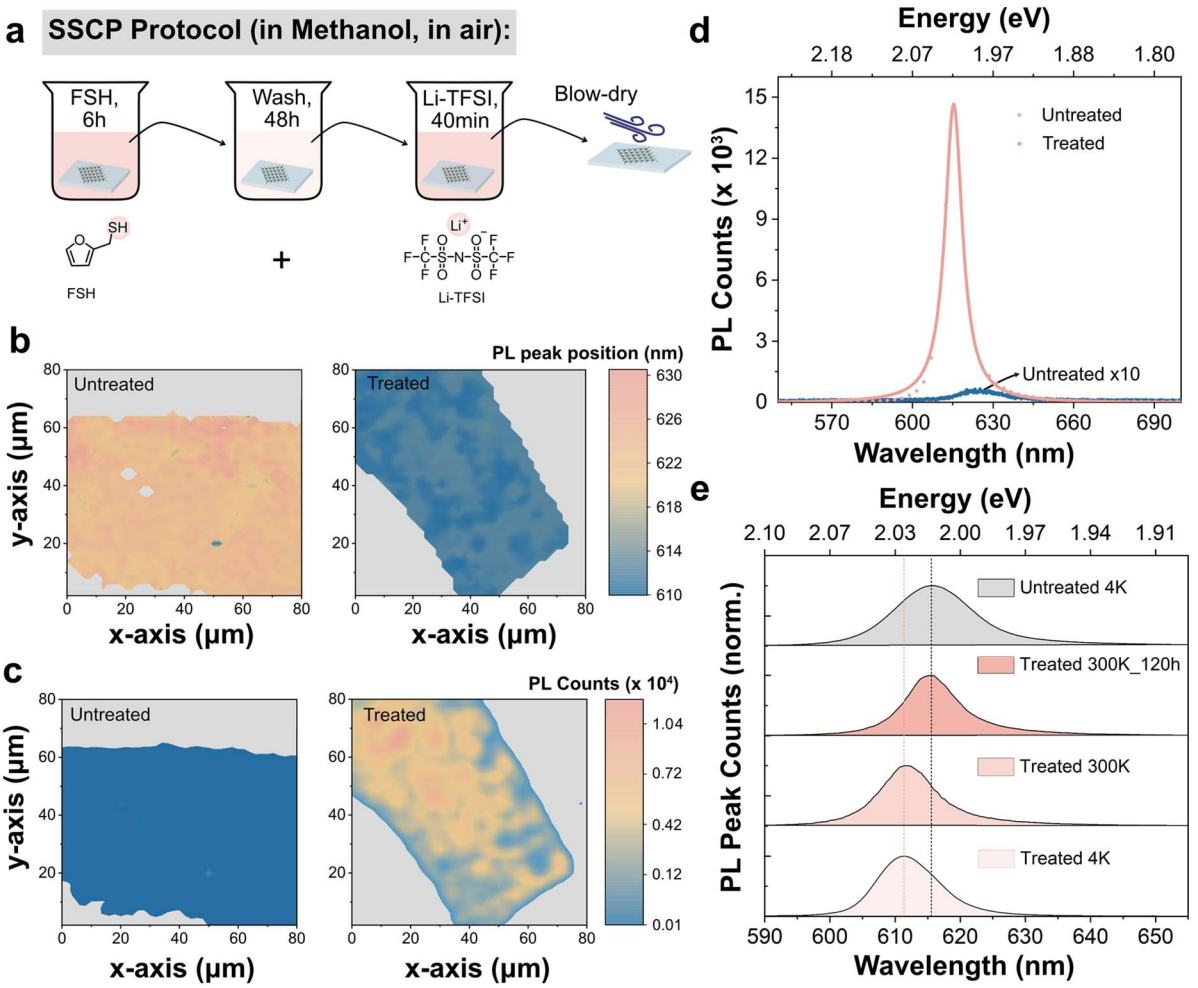

Fig. 1. Illustration of sequence-specific chemical passivation (SSCP) protocol and photoluminescence (PL) enhancement on monolayer WS_2. a Illustration of the developed sustainable SSCP protocol procedure, and the structures of the chemicals for the treatment (FSH + Li-TFSI). **b** Mapping of the PL peak position of untreated and treated samples. **c** Mapping of the PL intensity of untreated and treated samples. **d** Representative PL spectra for untreated and treated monolayer WS_2. **e** Normalized PL spectra for the untreated and treated sample at 4K compared with the normalized PL spectra for treated and stabilized treated sample (after treatment 120h) at 300K.

To understand the binding chemistry between chemicals and the 2D WS_2 surface, we initially modified the chemical treatment procedures and evaluated the resultant changes in the PL spectra of 2D WS_2 (Fig. S5 – S8) As shown in Fig. S5, following the FSH treatment, we observe a homogeneous enhancement in the PL peak intensity across the monolayer flake of 2D WS_2. This is in contrast to the inhomogeneous shift in the PL peak position (For a detailed discussion, refer to Supplementary Information Note 4). The subsequent treatment with Li-TFSI results in an inhomogeneous enhancement of PL intensity across the WS_2 monolayer flake. This indicates

that FSH and Li-TFSI interact differently with the WS_2 surface, potentially passivating distinct types of defects.

Additionally, it is worth noting that the PL peak position exhibits a slower response rate to the washing procedure (Fig. S6). Following a 24-hour immersion of the treated sample in Methanol solvent, the PL peak positions maintain relative stability across the monolayer flakes. This behavior is in stark contrast with the PL intensity of the treated sample, which experiences a significant decrease after the 24-hour immersion in the Methanol solvent. This differential sensitivity of the PL peak position and intensity to the rinsing procedure suggests a complex interplay of factors governing these properties. Moreover, as depicted in Fig. S7 and S8, the subsequent Li-TFSI treatment process reveals a gradual enhancement and blueshift in the emission of 2D WS_2. Interestingly, this enhancement in PL intensity, induced by the Li-TFSI treatment, exhibits a level of reversibility, suggesting the absence of any chemical reactions between FSH and Li-TFSI, as well as between Li-TFSI and the surface of 2D WS_2. Based on these observations, we hypothesize that the developed treatment protocol contributes to improved p-doping and alteration of the electronic structure of 2D WS_2, leading to the observed furthest blueshift and largest intensity enhancement, respectively.

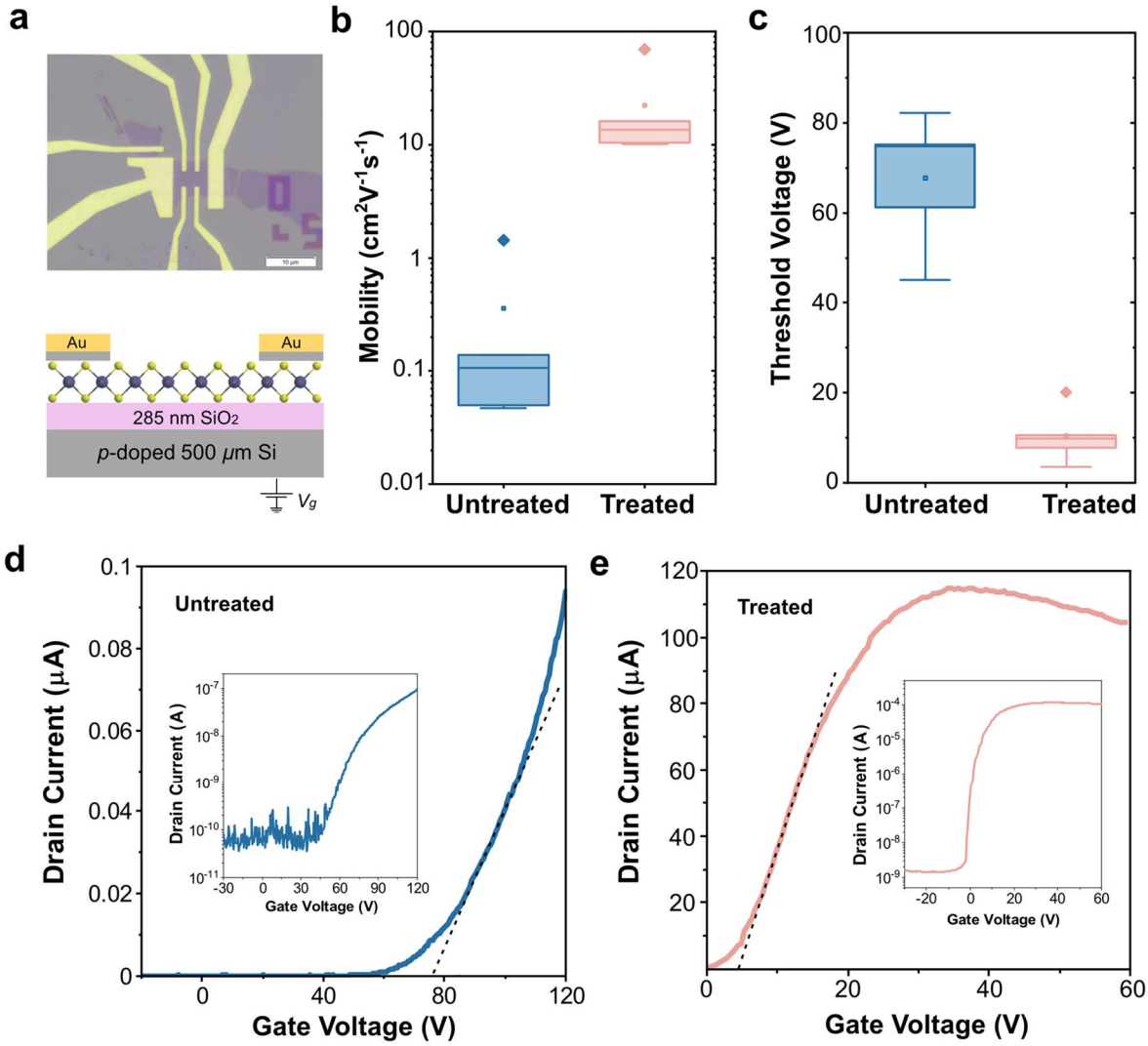

Fig. 2. Electrical measurements. a Optical image (top) and schematic representation (bottom) of as-fabricated monolayer WS_2 field-effect transistor (FET) device with Ti (5 nm) and Au (55 nm) contacts prepared using e-beam lithography patterning and electron beam metal evaporation. Scale bar, 10 μm. **b** Field-effect mobility for FET devices before and after treatment, plotting the mean (solid line) and standard deviation (box) on different devices. **c** Threshold voltage shift for FET devices before and after treatment. **d** Drain current versus gate voltage of untreated monolayer WS_2 at drain-source voltage (V_{DS}) of 1V in linear scale. Inset: in logarithmic scale. **e** Drain current versus gate voltage of treated monolayer WS_2 at V_{DS} of 1V. Inset: in logarithmic scale.

Besides PL, the charge-carrier mobility is a measure of semiconductor quality since it is very sensitive to impurities and traps. Here, we fabricated field-effect transistors (FETs) of WS_2 monolayers and characterized the field-effect transport properties before and after treatment

(Fig. 2a). The electrical characterizations of transistors were conducted in a high-vacuum environment (~10^{-7} mbar) to eliminate extrinsic doping effects induced by air or moisture. The detailed parameters for untreated and treated devices are presented in SI Note 5 (Table S1 and S2, and Fig. S9 and S10). As depicted in Fig. 2b, we observe a striking two-order increase in the field effect mobility, reaching up to 70 cm^2 V^{-1} s^{-1} at room temperature. This is the highest value achieved for mechanically exfoliated WS_2 monolayer on SiO_2 substrates. Such an enhancement can be attributed to the passivation of the sulfur vacancy sites, which is expected to reduce the long-range coulomb scattering. The treated FETs exhibit an average field-effect charge mobility of ~ 12 cm^2 V^{-1} s^{-1}, while that of untreated FETs is ~ 0.1 cm^2 V^{-1} s^{-1}. At the same time, we also observe small variations that can originate from different channel lengths.[37]

In addition to the 2-order enhancement in mobility upon passivation, we observe a clear decrease in the threshold voltage (V_T) after the chemical treatment (Fig. 2c). The V_T is extracted using the Extrapolated Linear Region (ELR) method, as illustrated in Fig. 2 d and e. Statistically, the V_T values for the treated transistors were found to be 12 ± 8 V, while the untreated transistors exhibited a larger variation, with values lying in the range of 64 ± 19 V. This shift can be attributed to the p-doping effect from the Li^+ ion, which is expected to decrease the concentration of trions thereby facilitating easier charge transfer across source and drain terminals. This Fermi-level shift in 2D WS_2 aligns well with the PL measurements discussed above, and the DFT simulation discussed later. Notably, our SSCP protocol leads to a three-order-of-magnitude decrease in the total FET resistance. The electrical measurements suggest a synergistic effect of increased doping and sulfur vacancy defect passivation due to the SSCP.

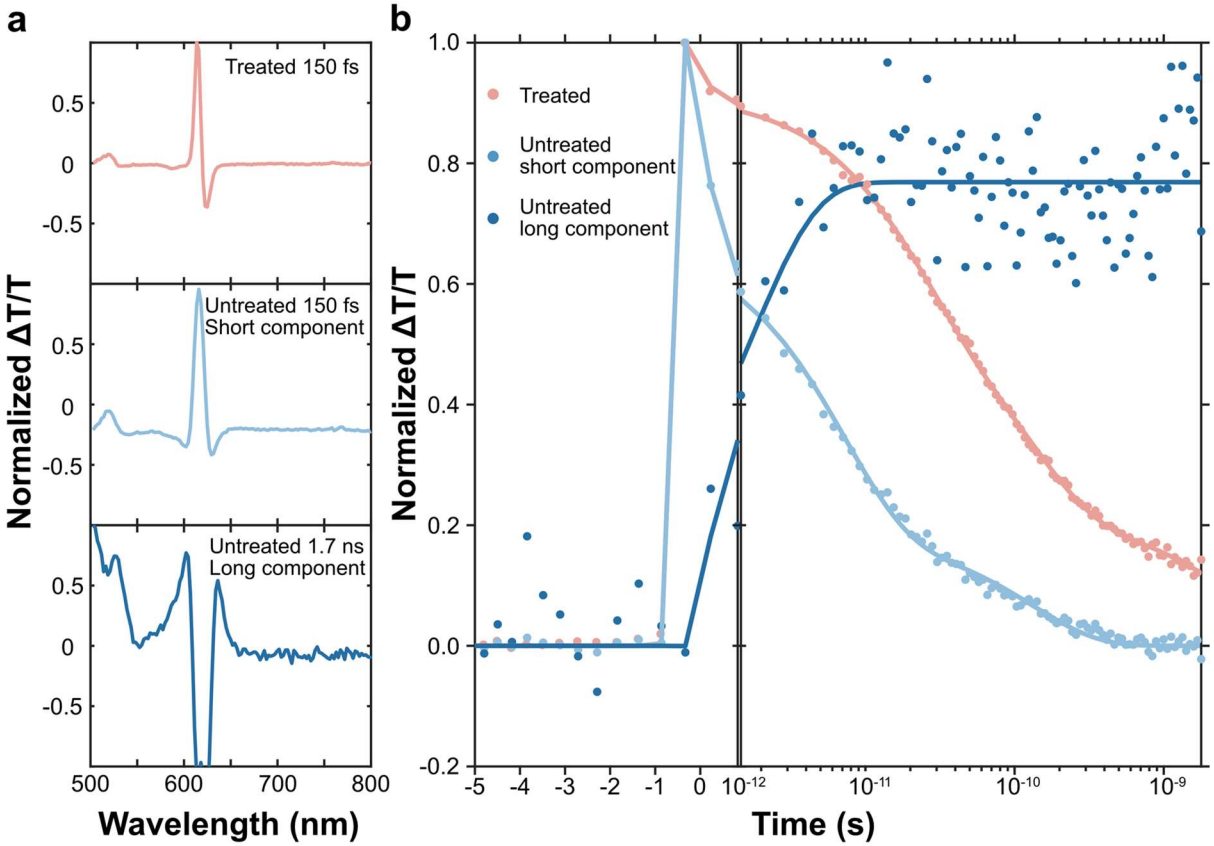

Fig. 3. Pump-probe spectra and excited state dynamics of untreated and treated monolayer WS_2. a Normalized pump-probe spectra of treated and untreated monolayer WS_2 at 150 fs, and normalized pump-probe spectrum at 1.7 ns for untreated monolayer WS_2. **b** Kinetic profiles for the corresponding spectra in **a** and multi-exponential fits using a 185-fs-wide Gaussian response function. The fitting is presented in solid lines.

To further understand the effect of chemical treatment on the optical and electronic properties we studied the WS_2 monolayers using fs-transient absorption (fs-TA). It measures the change in transmission after the sample is excited by a ~200 fs laser pulse. In our experiments, a positive $\frac{\Delta T}{T}$ signal corresponds to when the excited sample transmits more light due to the depopulation of the ground state, referred to as ground state bleach (GSB). Negative $\frac{\Delta T}{T}$ signals can arise due to the absorption of an excited state (photoinduced absorption, PIA) or the stimulated emission (SE) from the excited state. We compared multiple untreated monolayers to understand the sample variations (Fig. S11). All samples show similar spectral features and only minor differences in decay dynamics. It is clear that for the untreated samples, two spectral components are observed. This is also supported by single value decomposition (SVD) of the experimental dataset where two components show significantly larger singular values and

spectral components above the noise level (detail in Supplementary Note 6, Fig. S12 and S13). From the TA data, we can identify an initial spectrum (100 fs – 1 ps) with a positive peak corresponding to the A-exciton GSB at 616 nm (Fig. 3 and S14) and another peak from the B-exciton GSB at 520 nm. Over the first 10 ps, these features disappear and a broad positive feature between 600-650 nm arises with a sharp negative peak overlapping at 620 nm. The dynamics of the spectral components are extracted using spectra at early (150 fs) and long (1.7 ns) times, as detailed in Supplementary Note 6. The initial component exhibits an average lifetime of 1-5 ps across two independent samples, with the emergence of a broad feature occurring concurrently. The broad feature is similar to that observed in liquid-exfoliated WS_2 in our previous work.[38] We previously assigned this broad feature to the GSB of multilayer WS_2 arising due to energy transfer. However, as the prepared mechanically exfoliated samples here do not have any multilayer parts (Fig S1c) this feature must be associated with something else. We assign this to the GSB of a charged sulfur vacancy trap state which is supported by our DFT simulation as we discuss subsequently.

Interestingly, a comparison of the trap-state feature signal at 1.7 ns reveals a relatively minor dependence on intensity. In Fig. S11, we compare the signal between low (50W) and high (360W) excitation. Despite a more than seven-fold increase in excitation intensity, the initial GSB increases proportionally, while the trap-state signal only doubles. This suggests a limited number of traps that can be populated from the initial excited state. A similar observation is made when the excitation is changed from 610 nm to 510 nm, where the sample's higher absorption leads to a greater initial excited state population and GSB signal. However, the trap-state signal remains consistent with that observed with 610 nm excitation. Following the SSCP protocol, the initial GSB signal experiences a slight blueshift to 614 nm, with only one spectral component observed (refer to Fig. 3 and S15). Simultaneously, the GSB signal decays with an average lifetime of 31 ps, an order of magnitude slower compared to the untreated samples. These observations collectively provide clear evidence that the SSCP protocol developed in this study effectively passivates (removes) the sulfur vacancy trap states in 2D WS_2, thereby extending the excited state lifetime and slowing the decay dynamics. This explains the observed increase in PL photon intensity and charge carrier mobility.

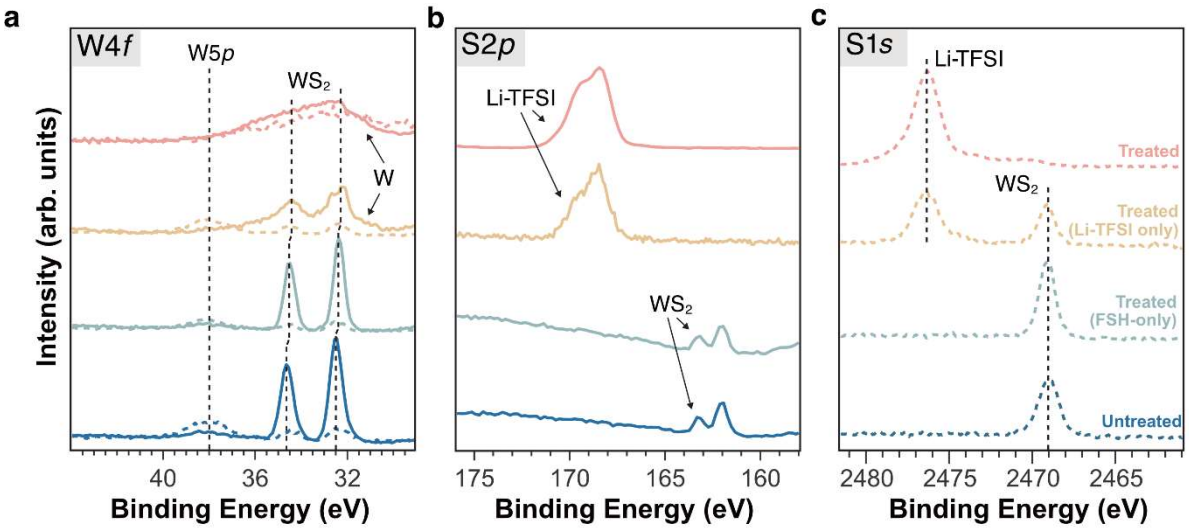

Fig. 4. X-ray Photoelectron Spectroscopy (XPS) and Hard X-ray Photoelectron Spectroscopy (HAXPES) measurements. Core levels of **a** W4f, **b** S2p, and **c** S1s before and after surface treatments. Spectra displayed with dotted lines are measured with HAXPES.

To determine the stoichiometry of untreated and treated WS_2 monolayers, we employed the XPS and HAXPES. The W4*f* and S2*p* core level photoelectron spectra were analyzed and the ratio of the two core level areas was compared before and after surface treatment (Fig. 4). The area of the respective peak was obtained from the fit after background subtraction, using curve fitting. The Scofield ionization cross-section values for the respective core levels were taken into account (1.68 for S2*p* and 9.80 for W4*f*).[39] The S/W ratio was found to be 1.81 for the untreated WS_2 sample and 2.43 for the sample treated with FSH. The increase in the relative amount of sulfur suggests that the sulfur from the FSH surface treatment fills some of the SVs in the WS_2 monolayer. The sulfur 2*p* core level spectra, as depicted in Fig. 4b, reveal a WS_2 binding energy of 162.0 eV ($2p_{3/2}$ component) for both untreated WS_2 and the FSH-treated sample. In the case of treated sample and sample treated with Li-TFSI only, sulfur peaks originating from Li-TFSI are observed. These peaks exhibit similar binding energies, with a minor shift of 0.1 eV between the two samples ($2p_{3/2}$ component at 168.4 eV and 168.3 eV, respectively), indicating that there is no chemical reaction with Li-TFSI treatment.[40,41] This is further supported by the HAXPES measurement showing that The S1*s* peak originating from the WS_2 layer (2470.1 eV) is consistent across the untreated WS_2, the FSH treated, and the Li-TFSI-only treated sample (Fig. 4c). The overall XPS spectra of WS_2 before and after varied treatments with detailed discussion can be found in Supplementary Note 7, Fig. S16 and the core-level binding energies are summarized in Table S4. Overall, these XPS and HAXPES data

indicate the effective passivation of the new chemical protocol without necessitating the chemical modification of the WS_2 monolayer.

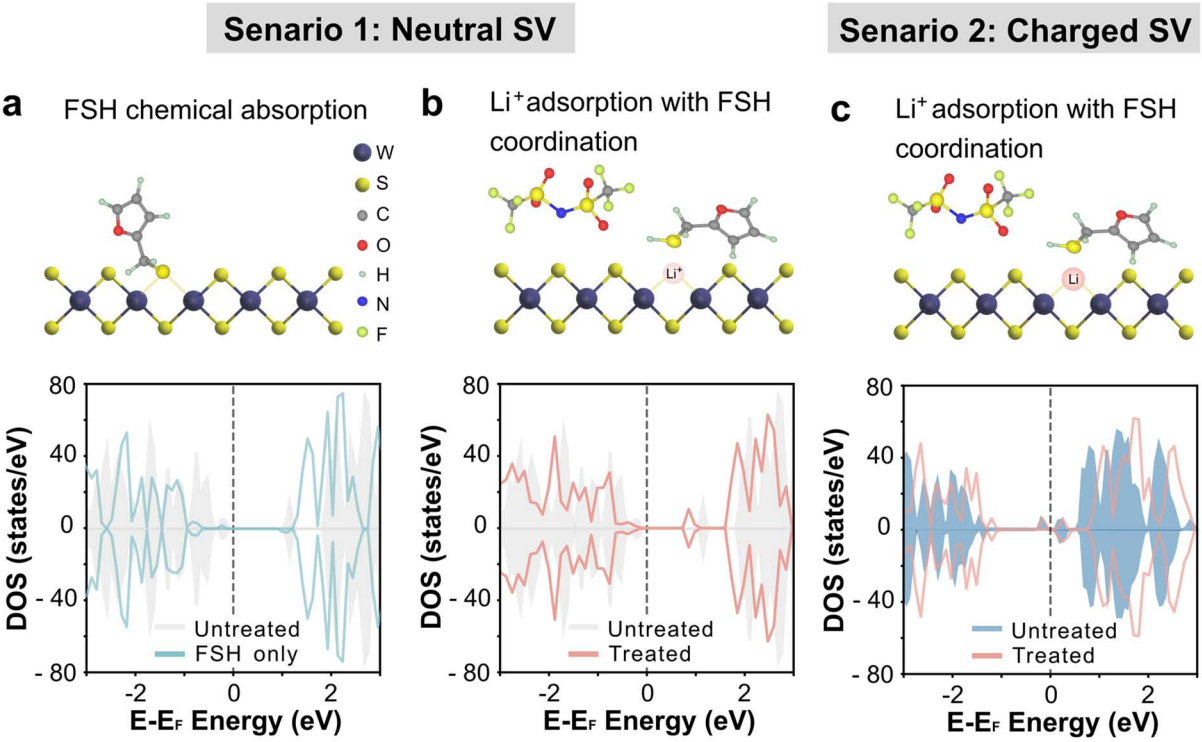

Fig. 5. Atomic structures and DFT calculation results of the effect of chemical passivation. **a** Schematic picture of the chemisorbed FSH together with the summed projected density of states (PDOS) as a function of energy relative to the Fermi level on the 2D WS_2 layers before and after the chemisorption while a neutral SV is considered. **b** Schematic picture of the FSH molecule coordinating Li^+ adsorption and the summed PDOS on the 2D WS_2 layers before and after the adsorption while a neutral SV is considered. **c** The summed PDOS on the 2D WS_2 layers before and after the adsorption while a charged SV is considered.

To obtain insights into the mechanisms of SVs passivation on the WS_2 monolayers by synergetic chemical treatment, we performed the ab initio density functional theory (DFT) calculations to gain insights into the mechanisms of sulfur vacancies (SVs) passivation on the WS_2 monolayers by the synergetic chemical treatment. Summed PDOS calculations on atoms of the 2D layer were performed for various scenarios, encompassing the presence of cation (Li^+), anion ($TFSI^-$), and physisorbed thiols on top of the WS_2 monolayer. Both neutral (Fig. S17) and negatively charged SV defects (Fig. S18) were considered in these scenarios. Bader analysis was employed to deduce the insertion or removal of electrons within the layer. Our

DFT calculations reveal that the FSH molecule effectively saturates the 2D WS_2 surface, thereby reducing the presence of the solvent methanol due to their strong van der Waals interactions with the WS_2 monolayer. When a thiol group attaches to the monolayer surface, the S-H bond can cleave, depending on the local environment. This initiates chemical absorption of the remaining S onto neutral SV defects, which alters the electronic structure of the 2D layer, resulting in shallower defective states. (Fig. 5a, Fig. S19). The sulfur absorption process is less likely to occur in negatively charged SV defects due to lower adsorption energies between the cleaved molecule and the negatively charged defect. Following treatment with Li-TFSI, lithium cation (Li+) stably adsorbs onto both the negatively charged defects and neutral defects (Fig. 5b, 5c, and Video S1, S2). Notably, for the neutral SV defect, changes in the summed PDOS of the layer were observed exclusively when FSH coordinated with Li+. By comparing with the TA data, the sub-gap of untreated 2D WS_2 is closer to the band edge, which is responsible for the broader absorption feature in the TA measurements. Li-TFSI treatment shifts the band gap for negatively charged SV away from the conduction band edge, making the repopulation of charges from the trap state unlikely. Furthermore, Bader charge analysis revealed a reduction of 0.11 electrons for Li^+ adsorption in the negatively charged SV defect, while in the scenario involving neutral SV defects, 0.08 fewer electrons were observed when Li^+ was coordinated by the FSH molecule. The calculations do not reveal any electron insertion or removal from the layer in other cases (detailed discussion in SI Note 8, Table S5, Fig. S20).

Overall, the neutral SV defects are likely to be populated by cleaved FSH molecules with S atoms and Li^+ adsorption coordinated by FSH. In contrast, for negatively charged SV defects, FSH-coordinated Li^+ adsorption dominates. Our experiments and the DFT calculations reveal that this synergistic binding chemistry, involving such adsorptions and electron extraction from the 2D WS_2 layer, leads to the passivation of defect trap states, resulting in the observed enhancement in PL and electrical mobility.

Conclusion

Through our innovative SSCP protocol, we have achieved a remarkable amplification of the PL in WS_2 monolayers, increasing it by up to 200 times. This enhancement is characterized by a narrower FWHM and a significant blue shift in the PL peak position, aligning with low-temperature PL measurements that indicate intrinsic PL behavior. Additionally, our treatment has resulted in a 100-fold increase in charge mobility at room temperature, reaching values up to 70 $cm^2\ V^{-1}\ s^{-1}$ at room temperature. Our large-area and high quality WS_2 monolayer samples

have enabled comprehensive characterizations including ultrafast transient absorption spectroscopy and X-ray photoelectron spectroscopy (XPS), which unequivocally confirmed the effectiveness of the defect passivation. The DFT calculations provide insights into these experimental results, revealing an atomic-level synergistic defect passivation mechanism. Specifically, FSH molecules are found to be chemically adsorbed in the presence of two neighboring SVs, and Li+ ions show enhanced stability on the 2D WS_2 surface when coordinated by the FSH molecules, under both neutral and charged SV conditions. Our work sets a new benchmark by simultaneously enhancing the optical and electronic properties of 2D WS_2. Moreover, our SSCP protocol is sustainable and suitable for integration into device fabrication. This research provides a robust framework for binding chemistry engineering, enabling precise manipulation of the optical and electronic properties of 2D WS_2 and paving the way for advanced applications in electronics and optoelectronics.

Methods

Material and Sample Preparation

Bulk WS_2 crystals were purchased from 2D Semiconductors. The monolayer WS_2 were prepared according to reported gold-mediated exfoliation method to ensure relatively large monolayers.[42] In this study, all experiments were carried out on monolayers. All chemicals for the surface treatments were purchased from Sigma-Aldrich and used as received.

Spectroscopic Characterization

The temperature dependent PL measurement is performed using an excitation wavelength 544 nm, excitation power: 150 μW, integral time 1 sec for untreated and H-TFSI-only treated samples. Excitation wavelength 561 nm, excitation power 150 μW, and integral time 1 sec are used for the treated sample. The microscope steady-state PL measurement was carried out using a WITec alpha 300 s setup and has been described previously.[43] Importantly, a 405 nm continuous wave laser (Coherent CUBE) was used as the excitation source. A long pass filter with a cutoff wavelength of 450 mm was fitted before signal collection to block excitation scatter. The light was coupled with an optical fiber to the microscope and focused using a 20× Olympus lens. Samples were placed on an X-Y piezo stage of the microscope. The PL signal was collected in refection mode with the same 20× objective and detected using a Princeton Instruments SP-2300i spectrometer fitted with an Andor iDus 401 CCD detector. The PL maps were measured at 405 nm excitation with a fluence of 15 W cm^{-2}. The Raman measurements were carried out using Renishaw inVia Raman confocal microscope with a 532 nm excitation

source. Transient absorption was performed on a setup described previously.[44] Details can be found in Supplementary Note 1. The X-ray Photoelectron Spectroscopy (XPS) measurement was employed using a Al-Kα radiation source at photon energy 1486.6 eV. For the HAXPES measurement, a Ga-Kα radiation source at 9252.8 eV photon energy was used. Details can be found in Supplementary Note 1.

FET device fabrication and measurements

The monolayer WS_2 flakes were mechanically exfoliated using the gold-mediated exfoliation method and transferred directly on top of a highly p-doped Si/SiO_2 (285 nm) substrate initially patterned with a network of alignment marks. The marks at the corner of the substrates are protected by the photoresist. Following up, the gold was etched in a solution of potassium monoidide, and the substrate was rinsed in isopropyl alcohol (IPA). The flakes were then identified by optical contrast, and source-drain electrodes were patterned by electron beam lithography. Prior to exposure, we spin-coated a bilayer-positive resist of MMA EL 9 and ARP 6200.13 on the substrate. The exposed pattern was developed using timed steps of hexyl acetate, methyl isobutyl ketone (MIBK)/IPA, and IPA. Following that, we evaporated 5 nm of Ti seeding layer and 55 nm of Au in a high vacuum chamber with e-beam evaporation. The fabrication was concluded with a lift-off in hot acetone at 70 ºC for 10 min, rinsing in IPA at room temperature for 5 min, and drying with nitrogen gas. Room temperature electrical measurements were carried out in a high vacuum cryostat ($\sim 10^{-7}$ mbar) cryostat using a SMU K2450 to control the back-gate voltage and source meter K2400 for source-drain bias.

Theoretical calculations

The density functional theory (DFT) calculations were performed using the Projected Augmented Wave (PAW) method to solve the Kohn-Shan equations as implemented in the Vienna Ab initio Simulation Package (VASP).[45,46] The spin-polarized generalized gradient approximation has been used with the Perdew, Burke, and Ernzerhof (PBE) parametrization to describe the exchange and correlation term of the Kohn-Sham Hamiltonian.[47] Moreover, the DFT+D3 approach was used to take into account the van der Waals interactions.[48,49] Details can be found in Supplementary Note 2.

Author Contributions

Z. L. designed and conducted the experiments of chemical treatments, and performed the 2D material exfoliation, and Raman and photoluminescence measurements. Z. L., U. N., H. N., and

M. V. K designed, conducted the device fabrication, performed the electrical measurements and analyzed data. E. B. performed XPS and HAXPES measurements and analyzed data with A. L.. Z. L. and V. G. performed transient absorption measurements and analyzed the data. T. K. and E. A. performed the temperature-dependent PL measurements and analyzed data with M. K. and Z.L.. R. A. designed and performed computational studies and analyzed with T. E.. Z. L., R. A., A. R., and M. V. K supervised the work. All authors contributed to the data analysis and writing of the manuscript.

Acknowledgments

This project has received funding from the Swedish Research Council, Vetenskapsrådet 2018-06610, 2023-05244, and ÅForsk Foundation nr. 22-390. The computations were enabled by resources provided by the National Academic Infrastructure for Supercomputing in Sweden (NAISS) via NAISS 2023/5-276 partially funded by the Swedish Research Council through grant agreement no. 2019-0559. This project has received funding from the European Research Council under the European Union's Horizon 2020 research and innovation program (Grant Agreement No. 758826 (SOLARX) to A.R.). European Research Council (ERC) Project SPINNER (Grant Agreement No. 101002772) and Formas (Grant Agreement no. 2023–01607) to M. V. K are acknowledged.

Competing interests

The authors declare no competing interests.

Supplementary Information

Supplementary Information is available online with additional experimental and calculation details as well as additional data for optical and electrical characterizations of 2D WS_2 samples and DFT simulations.

References

1. Huang, L. *et al.* Enhanced light–matter interaction in two-dimensional transition metal dichalcogenides. *Rep. Prog. Phys.* **85**, 046401 (2022).
2. Tan, C. *et al.* Recent Advances in Ultrathin Two-Dimensional Nanomaterials. *Chemical Reviews* **117**, 6225–6331 (2017).
3. Twenty years of 2D materials. *Nat. Phys.* **20**, 1–1 (2024).

4. Elahi, E. *et al.* Contemporary innovations in two-dimensional transition metal dichalcogenide-based P–N junctions for optoelectronics. *Nanoscale* **16**, 14–43 (2024).
5. Dai, Y., He, Q., Huang, Y., Duan, X. & Lin, Z. Solution-Processable and Printable Two-Dimensional Transition Metal Dichalcogenide Inks. *Chem. Rev.* **124**, 5795–5845 (2024).
6. Gao, L., Hu, Z., Lu, J., Liu, H. & Ni, Z. Defect-related dynamics of photoexcited carriers in 2D transition metal dichalcogenides. *Physical Chemistry Chemical Physics* **23**, 8222–8235 (2021).
7. Rhodes, D., Chae, S. H., Ribeiro-Palau, R. & Hone, J. Disorder in van der Waals heterostructures of 2D materials. *Nature Materials* **18**, 541–549 (2019).
8. Wang, S., Robertson, A. & Warner, J. H. Atomic structure of defects and dopants in 2D layered transition metal dichalcogenides. *Chemical Society Reviews* **47**, 6764–6794 (2018).
9. Mak, K. F. *et al.* Tightly bound trions in monolayer MoS2. *Nature Materials* **12**, 207–211 (2013).
10. Kato, T. & Kaneko, T. Transport dynamics of neutral excitons and trions in monolayer WS2. *ACS Nano* **10**, 9687–9694 (2016).
11. Cadiz, F. *et al.* Well separated trion and neutral excitons on superacid treated MoS2 monolayers. *Applied Physics Letters* **108**, (2016).
12. Lin, J. D. *et al.* Electron-doping-enhanced trion formation in monolayer molybdenum disulfide functionalized with cesium carbonate. *ACS Nano* **8**, 5323–5329 (2014).
13. Li, Z. *et al.* Efficient strain modulation of 2D materials via polymer encapsulation. *Nature Communications* **11**, 1–8 (2020).
14. Cadiz, F. *et al.* Excitonic linewidth approaching the homogeneous limit in MoS2-based van der Waals heterostructures. *Physical Review X* **7**, 1–12 (2017).
15. Cho, K., Pak, J., Chung, S. & Lee, T. Recent Advances in Interface Engineering of Transition-Metal Dichalcogenides with Organic Molecules and Polymers. *ACS Nano* **13**, 9713–9734 (2019).
16. Li, Z., Bretscher, H. & Rao, A. Chemical passivation of 2D transition metal dichalcogenides: strategies, mechanisms, and prospects for optoelectronic applications. *Nanoscale* 10.1039.D3NR06296A (2024) doi:10.1039/D3NR06296A.
17. Bianchi, M. G., Risplendi, F., Re Fiorentin, M. & Cicero, G. Engineering the Electrical and Optical Properties of WS_2 Monolayers via Defect Control. *Advanced Science* **11**, 2305162 (2024).
18. Sovizi, S. *et al.* Plasma Processing and Treatment of 2D Transition Metal Dichalcogenides: Tuning Properties and Defect Engineering. *Chem. Rev.* **123**, 13869–13951 (2023).
19. Michail, A. *et al.* Tuning the Photoluminescence and Raman Response of Single-Layer WS_2 Crystals Using Biaxial Strain. *J. Phys. Chem. C* **127**, 3506–3515 (2023).
20. Jang, J. *et al.* Reduced dopant-induced scattering in remote charge-transfer-doped MoS_2 field-effect transistors. *Sci. Adv.* **8**, eabn3181 (2022).

21. Zheng, W. *et al.* Light Emission Properties of 2D Transition Metal Dichalcogenides: Fundamentals and Applications. *Advanced Optical Materials* **6**, 1–29 (2018).
22. Liang, Q., Zhang, Q., Zhao, X., Liu, M. & Wee, A. T. S. Defect Engineering of Two-Dimensional Transition-Metal Dichalcogenides: Applications, Challenges, and Opportunities. *ACS Nano* **15**, 2165–2181 (2021).
23. Zhu, Y. *et al.* Room-Temperature Photoluminescence Mediated by Sulfur Vacancies in 2D Molybdenum Disulfide. *ACS Nano* **17**, 13545–13553 (2023).
24. Bertolazzi, S., Gobbi, M., Zhao, Y., Backes, C. & Samorì, P. Molecular chemistry approaches for tuning the properties of two-dimensional transition metal dichalcogenides. *Chemical Society Reviews* **47**, 6845–6888 (2018).
25. Carozo, V. *et al.* Optical identification of sulfur vacancies: Bound excitons at the edges of monolayer tungsten disulfide. *Science Advances* **3**, 1–10 (2017).
26. Bao, W. *et al.* Visualizing nanoscale excitonic relaxation properties of disordered edges and grain boundaries in monolayer molybdenum disulfide. *Nature Communications* **6**, 1–7 (2015).
27. Barja, S. *et al.* Identifying substitutional oxygen as a prolific point defect in monolayer transition metal dichalcogenides. *Nature Communications* **10**, 1–8 (2019).
28. Amani, M. *et al.* Near-unity photoluminescence quantum yield in MoS2. *Science* **350**, 1065–1068 (2015).
29. Bretscher, H. *et al.* Rational Passivation of Sulfur Vacancy Defects in Two-Dimensional Transition Metal Dichalcogenides. *ACS Nano* **15**, 8780–8789 (2021).
30. Li, Z. *et al.* Mechanistic insight into the chemical treatments of monolayer transition metal disulfides for photoluminescence enhancement. *Nature Communications* **12**, 6044 (2021).
31. Tarasov, A. *et al.* Controlled doping of large-area trilayer MoS2 with molecular reductants and oxidants. *Advanced Materials* **27**, 1175–1181 (2015).
32. Cong, C., Shang, J., Wang, Y. & Yu, T. Optical Properties of 2D Semiconductor WS_2. *Advanced Optical Materials* **6**, 1700767 (2018).
33. Currie, M., Hanbicki, A. T., Kioseoglou, G. & Jonker, B. T. Optical control of charged exciton states in tungsten disulfide. *Applied Physics Letters* **106**, 201907 (2015).
34. Mitioglu, A. A. *et al.* Optical manipulation of the exciton charge state in single-layer tungsten disulfide. *Phys. Rev. B* **88**, 245403 (2013).
35. Tongay, S. *et al.* Broad-range modulation of light emission in two-dimensional semiconductors by molecular physisorption gating. *Nano Letters* **13**, 2831–2836 (2013).
36. Zhang, Q. *et al.* Strain Relaxation of Monolayer WS_2 on Plastic Substrate. *Adv Funct Materials* **26**, 8707–8714 (2016).

37. Sebastian, A., Pendurthi, R., Choudhury, T. H., Redwing, J. M. & Das, S. Benchmarking monolayer MoS2 and WS2 field-effect transistors. *Nat Commun* **12**, 693 (2021).
38. Li, Z. *et al.* Understanding the Photoluminescence Quenching of Liquid Exfoliated WS_2 Monolayers. *J. Phys. Chem. C* **126**, 21681–21688 (2022).
39. Scofield, J. H. Hartree-Slater subshell photoionization cross-sections at 1254 and 1487 eV. *Journal of Electron Spectroscopy and Related Phenomena* **8**, 129–137.
40. Dedryvère, R. *et al.* XPS Valence Characterization of Lithium Salts as a Tool to Study Electrode/Electrolyte Interfaces of Li-Ion Batteries. *J. Phys. Chem. B* **110**, 12986–12992 (2006).
41. Leroy, S., Martinez, H., Dedryvère, R., Lemordant, D. & Gonbeau, D. Influence of the lithium salt nature over the surface film formation on a graphite electrode in Li-ion batteries: An XPS study. *Applied Surface Science* **253**, 4895–4905 (2007).
42. Desai, S. B. *et al.* Gold-Mediated Exfoliation of Ultralarge Optoelectronically-Perfect Monolayers. *Advanced Materials* **28**, 4053–4058 (2016).
43. Tainter, G. D. *et al.* Long-Range Charge Extraction in Back-Contact Perovskite Architectures via Suppressed Recombination. *Joule* **3**, 1301–1313 (2019).
44. Allardice, J. R. *et al.* Engineering Molecular Ligand Shells on Quantum Dots for Quantitative Harvesting of Triplet Excitons Generated by Singlet Fission. *Journal of the American Chemical Society* **141**, 12907–12915 (2019).
45. Kresse, G. & Furthmüller, J. Efficient iterative schemes for *ab initio* total-energy calculations using a plane-wave basis set. *Phys. Rev. B* **54**, 11169–11186 (1996).
46. Kresse, G. & Joubert, D. From ultrasoft pseudopotentials to the projector augmented-wave method. *Phys. Rev. B* **59**, 1758–1775 (1999).
47. Perdew, J. P., Burke, K. & Ernzerhof, M. Generalized Gradient Approximation Made Simple. *Phys. Rev. Lett.* **77**, 3865–3868 (1996).
48. Grimme, S., Antony, J., Ehrlich, S. & Krieg, H. A consistent and accurate *ab initio* parametrization of density functional dispersion correction (DFT-D) for the 94 elements H-Pu. *The Journal of Chemical Physics* **132**, 154104 (2010).
49. Grimme, S., Ehrlich, S. & Goerigk, L. Effect of the damping function in dispersion corrected density functional theory. *J Comput Chem* **32**, 1456–1465 (2011).

Supplementary Information

Synchronized Photoluminescence and Electrical Mobility Enhancement in 2D WS_2 through Sequence-Specific Chemical Passivation

Zhaojun Li*, Ulrich Noumbe, Elin Berggren, Henry Nameirakpam, Takashi Kimura, Eito Asakura, Victor Gray, Tomas Edvinsson, Makoto Kohda, Andreas Lindblad, Rafael Araujo*, Akshay Rao*, M. Venkata Kamalakar*

Contents

1. Supplementary Note 1 - experimental details 2

2. Supplementary Note 2 - calculation details 3

3. Supplementary Note 3 – Material characterization 3

4. Supplementary Note 4 - PL data for chemically treated monolayer WS_2 4

5. Supplementary Note 5 – FET device data 10

6. Supplementary Note 6 – Transient absorption spectroscopy data 14

7. Supplementary Note 7 – Photoelectron spectroscopy data 20

8. Supplementary Note 8 – DFT data 24

9. References 31

1. Supplementary Note 1 - experimental details

Si-SiO_2 substrates with 90 nm oxide layer were used for steady-state photoluminescence (PL), Raman spectroscopy and X-ray photoemission spectroscopy (XPS). Quartz substrates were used for ultrafast pump-probe measurement. All the measurements are carried out on samples without encapsulation.

Transient Absorption Spectroscopy measurement. A Light Conversion PHAROS laser system with 400 μJ per pulse at 1030 nm with a repetition rate of 38 kHz was used and the output was divided, one part was focused onto a 4 mm YAG substrate to produce a continuum probe beam from 520 to 950 nm. The second part of the PHAROS output was led into a narrow band optical parametric oscillator system (ORPHEUS-LYRA, Light conversion) outputting the pump beam. The probe pulse was delayed up to 2 ns with a mechanical delay stage (Newport). A mechanical chopper (Thorlabs) was used to create an on-off pump-probe pulse series. The pump size on the sample is approximately 0.045 mm^2 and the probe is about 0.008 mm^2. A silicon line scan camera (JAI SW-2000M-CL-80) fitted onto a visible spectrograph (Andor Solis, Shamrock) was used to record the transmitted probe light. The probe beam had a diameter of approximately half of the mechanically exfoliated monolayer size. Using a pin-hole to locate the monolayer the samples were placed to maximize the initial ground state bleach signal, ensuring that the probe was only probing the monolayer region. The pump was significantly larger than the monolayer to ensure uniform excitation across the whole monolayer. All obtained data was background and chirp corrected before analysis.

The X-ray Photoelectron Spectroscopy (XPS) measurement. Core levels and overview spectra were collected using a Scienta Omicron EW4000 hemispherical electron analyzer with a slit of 500 mm and a 200 eV pass energy. Binding energy calibration was obtained by aligning the Fermi level to a value of half the bandgap of monolayer WS_2, reported at 2.15 eV.[1] The experimental energy resolution was determined by the least squares fit of Au4*f* spectra using Voigt functions, employing 0.28 eV Au4$f_{5/2}$ and 0.3 eV Au4$f_{7/2}$ lifetime widths.[2] For XPS measurements this gave a Gaussian width of 0.62 eV and for HAXPES measurements at 0.88 eV. The Igor Pro 7.08 software and a CurveFitting procedure were employed to analyze the core level spectra [Edwin Kukk. Spectrum Analysis for Curve Fitting (SPANCF) macro package for Igor Pro.]. Voigt functions were utilized to fit the core level peaks, while the inelastic background was modeled using a Shirley function.[3]

2. Supplementary Note 2 - calculation details

The density functional theory (DFT) calculations. The density functional theory (DFT) calculations were performed using the Projected Augmented Wave (PAW) method to solve the Kohn-Shan equations as implemented in the Vienna Ab initio Simulation Package (VASP).[4,5] The spin-polarized generalized gradient approximation has been used with the Perdew, Burke, and Ernzerhof (PBE) parametrization to describe the exchange and correlation term of the Kohn-Sham Hamiltonian.[6] Moreover, the DFT+D3 approach was used to take into account the van der Waals interactions.[7,8] Plane waves were expanded to an energy cut-off of 520 eV while Γ point was used to sample the Brillouin zone. Here, it is important to emphasize that the lattice parameters of the employed supercells are a = 15.9 Å and b=15.9 Å with a vacuum of 20.0 Å to avoid periodic interaction between the layers. Forces convergence was set to 0.01 eV/Å while an energy convergence to 10^{-5} eV. Gibbs free energy variation of the adsorption energies was calculated as $\Delta G = \Delta E + \Delta ZPE + (\Delta H_{vib} + \Delta H_{rot} + \Delta H_{trans}) - T(\Delta S_{vib} + \Delta S_{rot} + \Delta S_{trans})$ where ΔZPE is the variation on the zero-point energy, ΔH and ΔS are the variations of enthalpy and entropy, respectively, and ΔE is the electronic energy change. Here, the final state is assumed to be the molecule + slab, while the initial state is the slab + molecule in the gas phase. For the gas-phase calculations, the molecules were placed in a box with a lattice parameter of 25 Å to avoid interaction between periodic images. Vibrational frequency calculations were performed using a finite difference approach.

3. Supplementary Note 3 – Material characterization

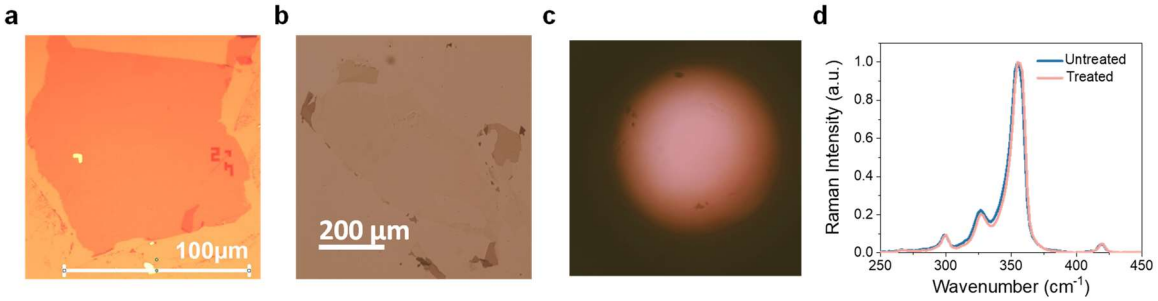

Supplementary Fig. 1 Characterization of mechanically exfoliated monolayer WS_2 samples. a Optical microscope image of a mechanically exfoliated WS_2 sample on Si/SiO_2 substrate. **b** Optical microscope image of mechanically exfoliated WS_2 sample 1 on a quartz substrate. **c** Optical microscope image of masked mechanically exfoliated WS_2 sample 1 on a

quartz substrate for transient absorption spectroscopy measurement. **d** Raman spectroscopy of mechanically exfoliated WS_2 samples on Si/SiO_2 substrate confirming the monolayer.

4. Supplementary Note 4 - PL data for chemically treated monolayer WS_2

Note that the "treated sample" without specification refers to 2D WS_2 treated with the developed protocol here. The PL spectra for H-TFSI-treated WS_2 monolayers at low temperature are not stable over time (blinking).

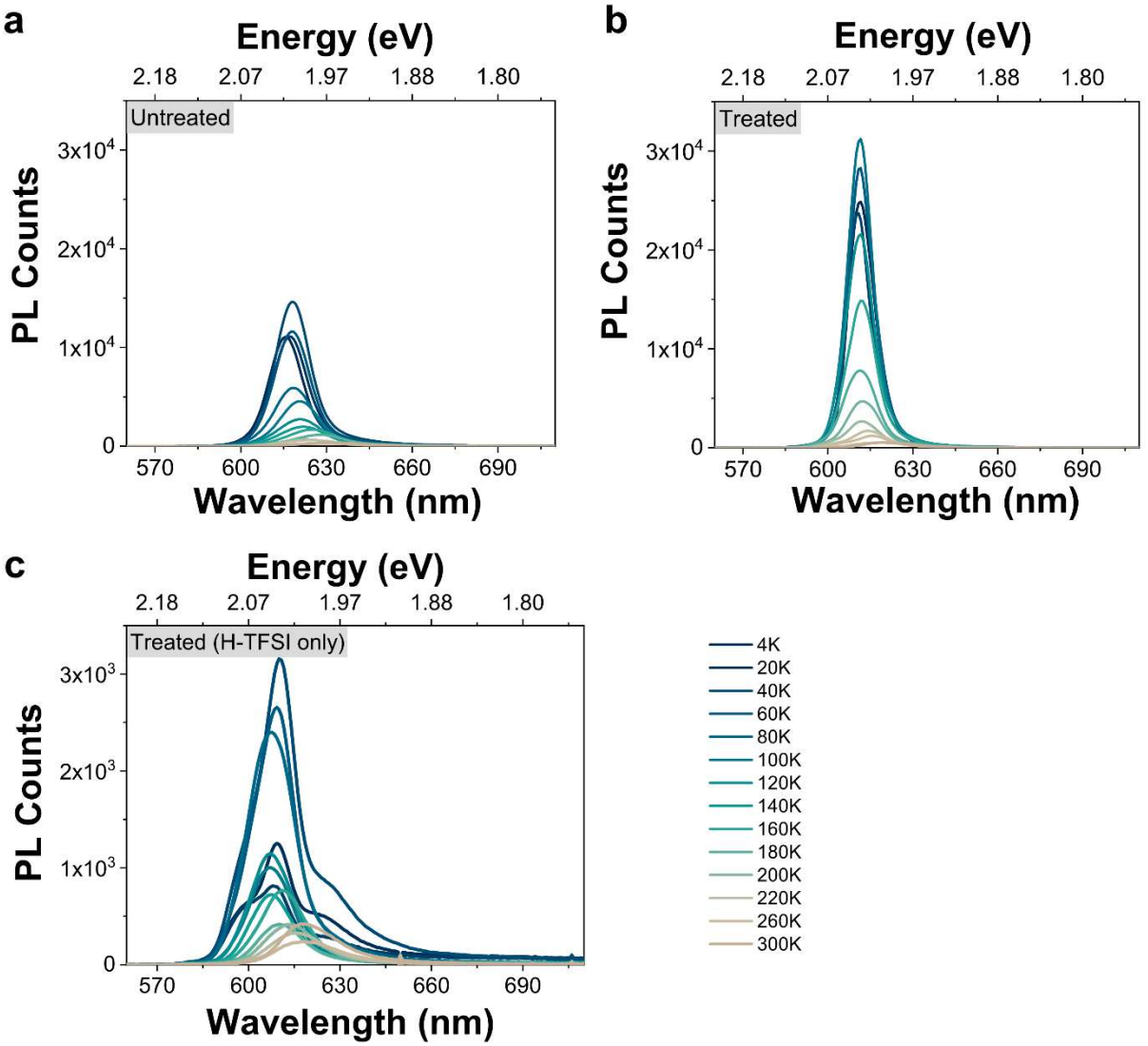

Supplementary Fig. 2 PL spectra measured for different temperatures on the untreated, H-TFSI-only treated, and treated monolayer WS_2 sample.

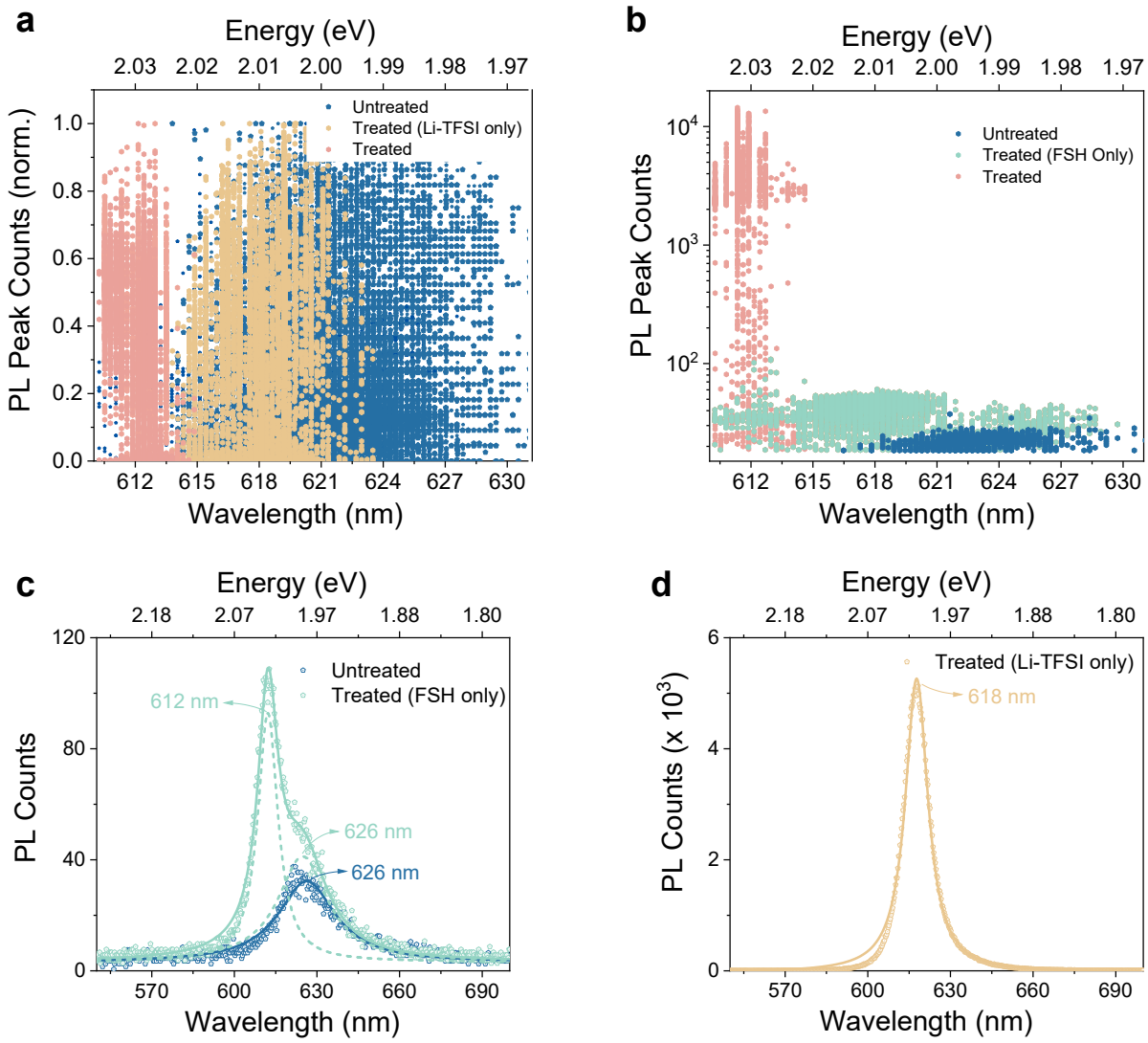

Supplementary Fig. 3 a Normalized PL peak counts and corresponding peak position of different samples with varied treatments. **b** Comparison of PL counts before and after treatments on the same sample. **c** Representative PL spectra for untreated and 2-furanmethanothiol (FSH)-treated monolayer WS_2. **d** Representative PL spectra for bis(trifluoromethane) sulfonimide lithium salt (Li-TFSI)-treated monolayer WS_2. The decomposed Lorentzian peak fitting is presented in dashed line and cumulative Lorentzian peak fittings are presented in solid line.

In Fig. S3 a and b, each dot signifies a PL spectrum, correlating the PL peak counts with the position of the PL maximum. The data is extracted from PL maps of WS_2 monolayers on Si-SiO_2 (90 nm), both before and after various surface treatments. Ten different untreated WS_2 monolayer flakes were mapped and normalized individually for this study (Fig. S3 a). Generally, the chemical treatments cause a blueshift in the PL spectra of the WS_2 monolayer,

with narrower variations in peak positions. Notably, the chemical treatment developed in this study causes the most significant blueshift in the PL spectra of the WS_2 monolayer, which is 20 meV more compared to treatments with H-TFSI or Li-TFSI alone. The PL peaks of treated WS_2 monolayers stabilize at 2.026 eV (612 nm) with variations around 10 meV. These findings suggest that the implemented treatment protocol enhances the p-doping effect and potentially minimizes defect occurrences, which are further supported by the charge mobility measurements, transient absorption spectroscopy measurements and DFT simulations.

The representative PL spectra of WS_2 monolayers, subjected to different treatments, are depicted in Fig. S3 c and d. The untreated WS_2 monolayers exhibit a dominant trion emission, peaking at 1.981 eV (626 nm). In contrast, the Li-TFSI-only treated sample shows a blue-shift in emission to 2.006 eV (618 nm). These results are consistent with our previous study.[9] The average treated PL intensity developed in this study is twice as high as that of Li-TFSI-only treatment.

The term 'FSH treatment' refers to the process wherein the WS_2 monolayer on a Si/SiO_2 substrate is immersed in a 0.01M FSH/Methanol solution for a duration of 6 hours. Subsequently, the sample is washed by immersion in a Methanol solvent for 48 hours, during which the solvent is periodically replaced. The FSH treatment results in a marginal enhancement of the PL intensity of the WS_2 monolayer. It is evident that the trion contribution remains strong, corresponding to the emission at 1.98 eV. However, a distinct excitonic emission peak emerges at 2.026 eV (612 nm), which suggests that more neutral excitons are populated and there is a suppression of non-radiative recombination. This peak is more blue-shifted compared to the Li-TFSI only treated sample and aligns with the peak position observed in the treatment protocol developed in this study. This indicates that the FSH treatment has contributed to defect passivation.

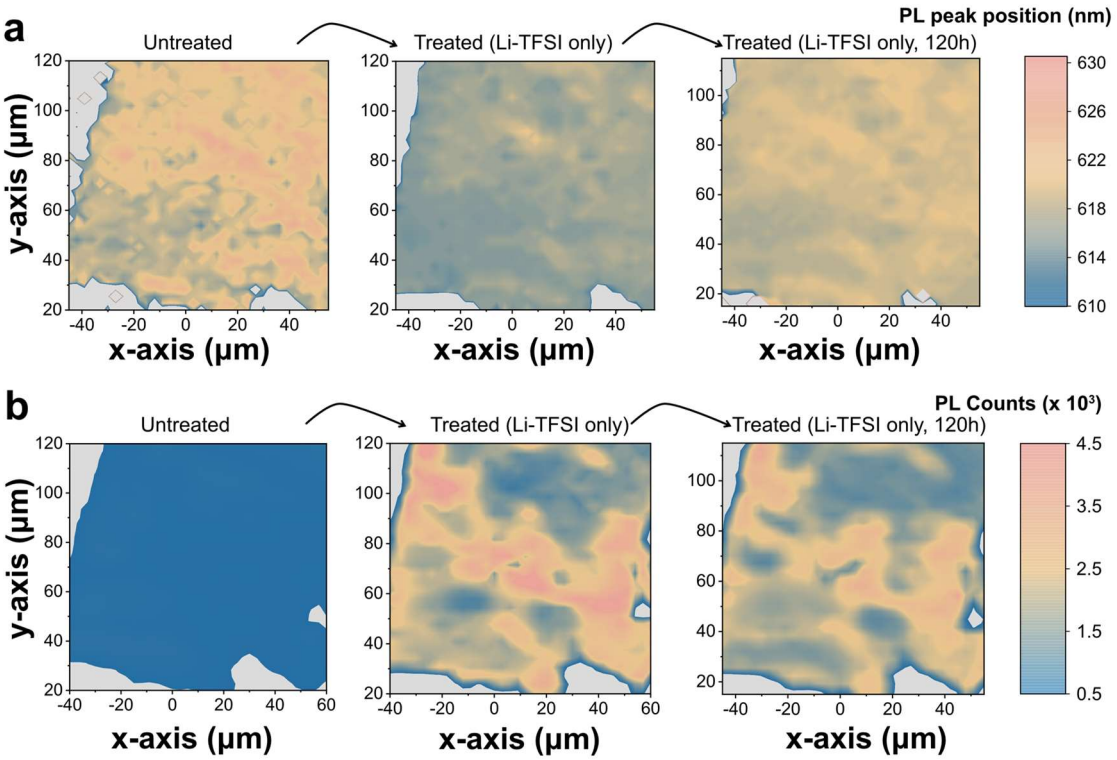

Supplementary Fig. 4 PL mapping of **a** PL peak position and **b** PL intensity change before and after the Li-TFSI only treatment on the same monolayer WS_2 sample. The PL spectra of the Li-TFSI treated sample undergo a redshift from 2.016 eV (615 nm) over time while stored in air, stabilizing at 2.003 eV (619 nm) with a position variation of 13 meV. This peak position shift is homogenous over the monolayer flake to a large extent.

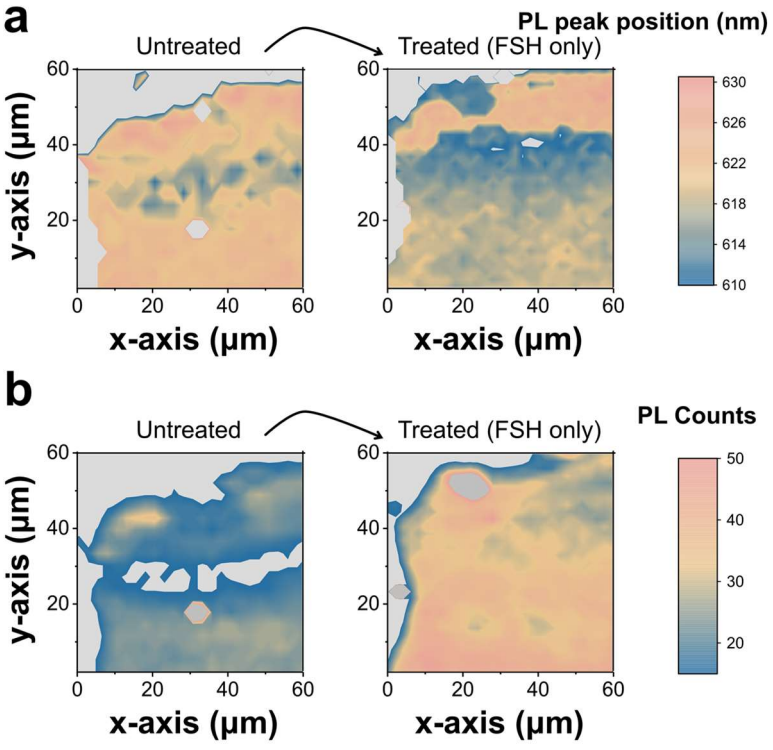

Supplementary Fig. 5 PL mapping of the PL peak position and PL intensity before and after the FSH treatment on the same monolayer WS_2 flake (sample 1).

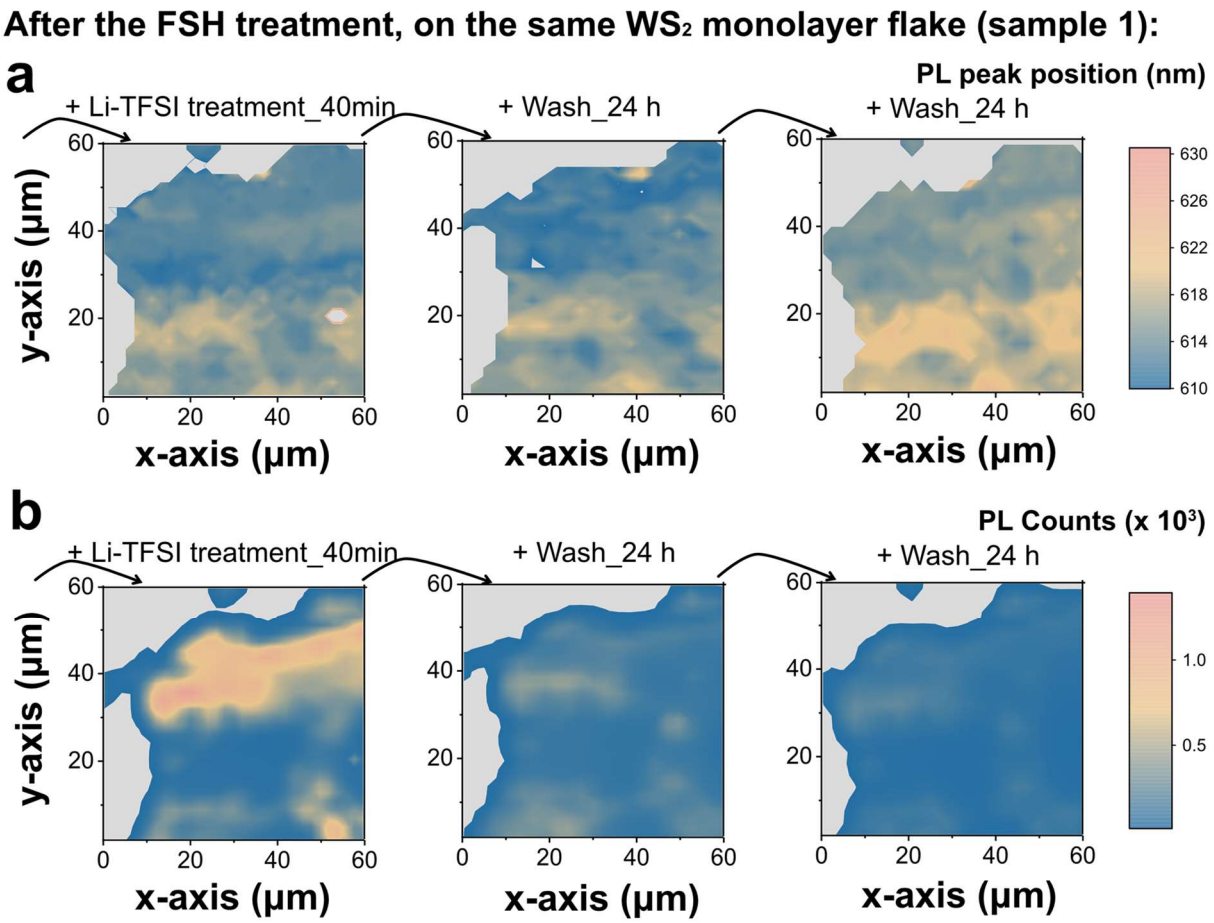

Supplementary Fig. 6 PL mapping of the PL peak position and PL intensity change after the chemical treatment and wash on the same monolayer WS_2 flake (sample 1).

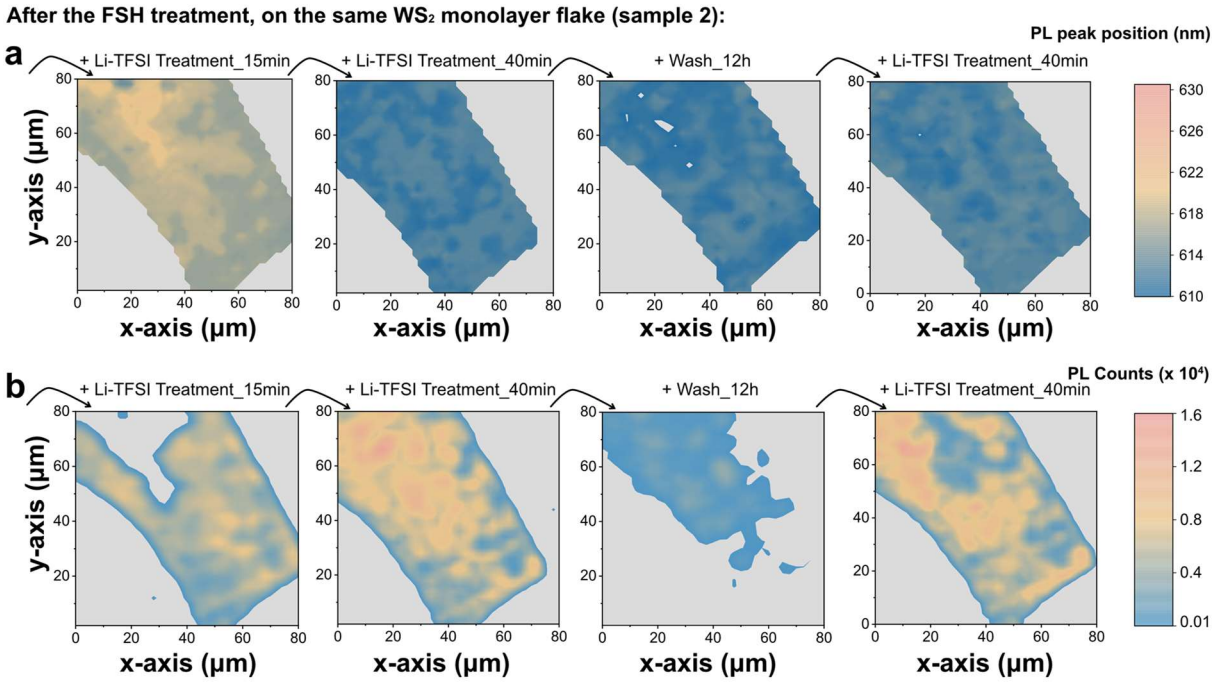

Supplementary Fig. 7 PL mapping of the PL peak position and PL intensity change during the subsequent Li-TFSI chemical treatments on the same monolayer WS_2 sample 2 after the FSH treatment.

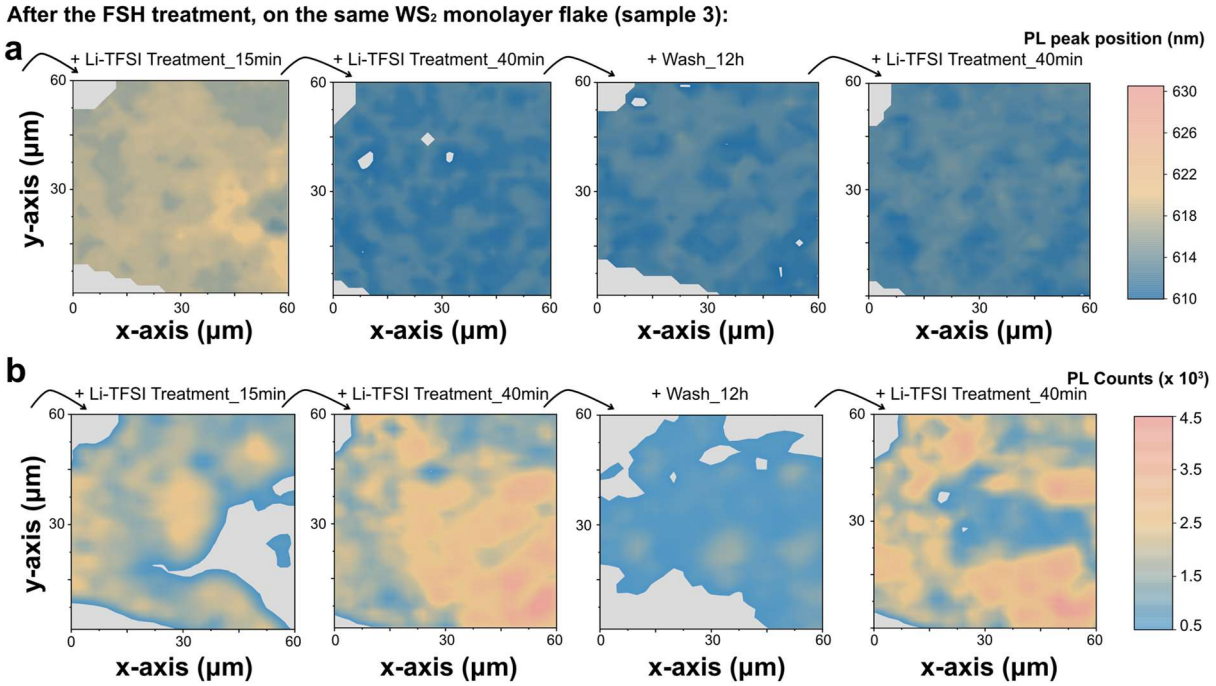

Supplementary Fig. 8 PL mapping of the PL peak position and PL intensity change during the subsequent Li-TFSI chemical treatments on the same monolayer WS_2 sample 3 after the FSH treatment.

5. Supplementary Note 5 – FET device data

We have fabricated and characterized five untreated FET devices and six treated FET devices at V_{DS} = 1 V. The detailed parameters are presented as follows:

Supplementary Table 1. Parameters from untreated monolayer WS_2 FET devices. Mobility is extracted at V_{DS} = 1 V. The threshold voltage is exacted in the Extrapolated Linear Region (ELR). The device 2 is used in the main text.

Device	**L_{ch} (µm)**	**W_{ch} (µm)**	**Mobility ($cm^2/(V \cdot s)$)**	**Threshold Voltage (V)**	**Total Resistance at V_g 120 V (R_T, Ohm)**	**Total Resistance at V_g 60 V (R_T, Ohm)**
1	0.88	3.33	0.0469	75.13	15.14M	76.92M
2	1.24	4.77	0.05	74.82	10.65M	1032.09M
3	1.16	4.04	0.107	45.05	3.35M	21.2M
4	1.5	4.34	0.139	61.28	3.88M	30.39M
5	7.32	7.29	1.433	82.09	1.57M	25.19M

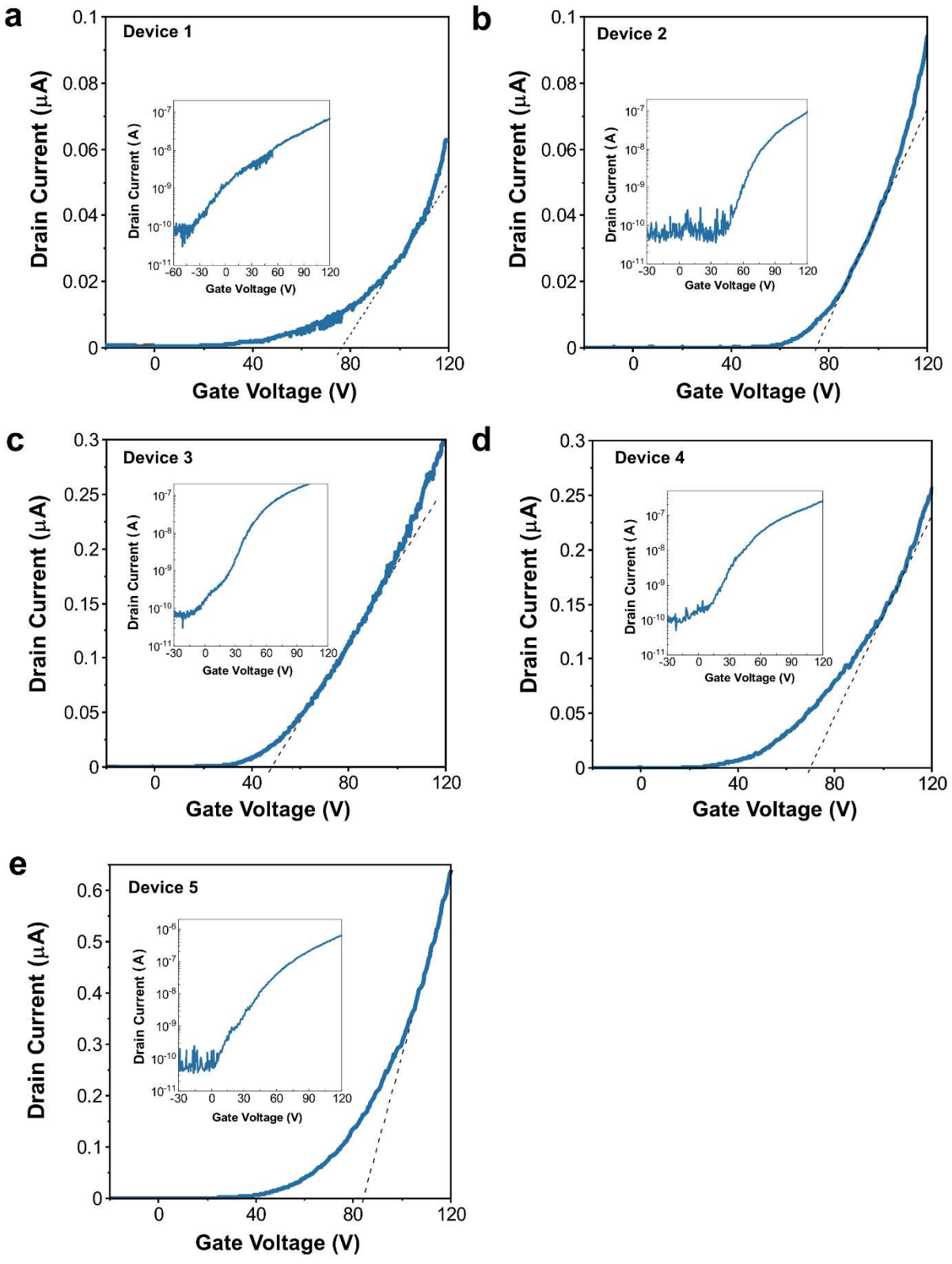

Supplementary Fig. 9 Drain current versus gate voltage of untreated monolayer WS_2 FET at drain-source voltage (V_{DS}) of 1V in linear scale. Inset: in logarithmic scale.

Supplementary Table 2. Treated devices. Mobility is extracted at V_{DS} = 1 V. The threshold voltage is exacted in the Extrapolated Linear Region (ELR). The device 6 is used in the main text.

Device	**L_{ch} (µm)**	**W_{ch} (µm)**	**Mobility ($cm^2/(V \cdot s)$)**	**Threshold Voltage (V)**	**Total Resistance at V_g 60 V (R_T, Ohm)**
6	2.09	16.62	69.73	3.51	9.4K
7	1.56	17.1	16.09	9.82	18.2K
8	1.15	7.59	14.85	10.62	51.3K
9	1.94	12.99	12.05	7.71	40.9K
10	0.9	10.29	10.08	20.08	29.3K
11	1.24	11.71	10.37	15.06	64.5K

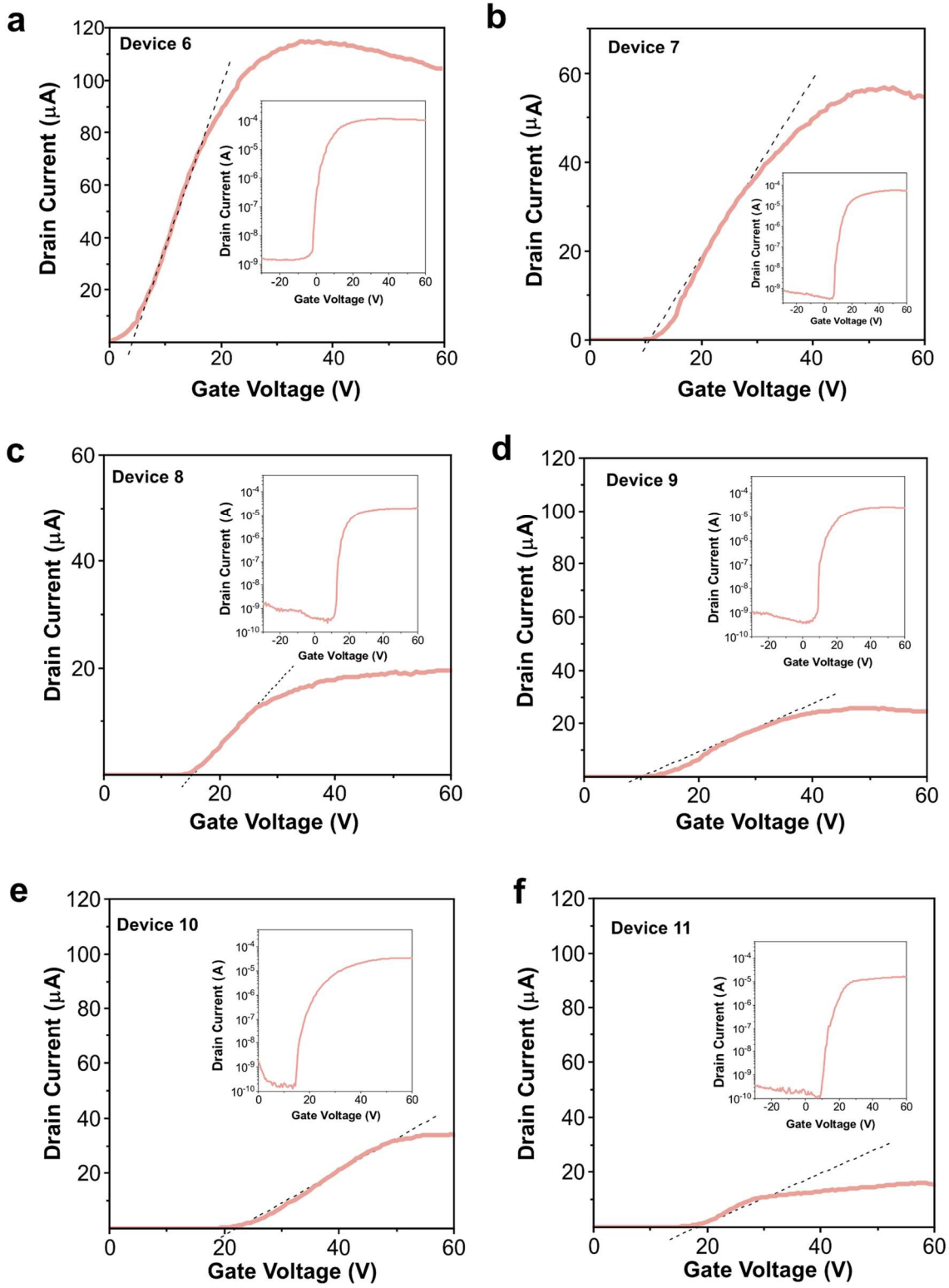

Supplementary Fig. 10 Drain current versus gate voltage of treated monolayer WS_2 FET at drain-source voltage (V_{DS}) of 1V in linear scale. Inset: in logarithmic scale.

6. Supplementary Note 6 – Transient absorption spectroscopy data

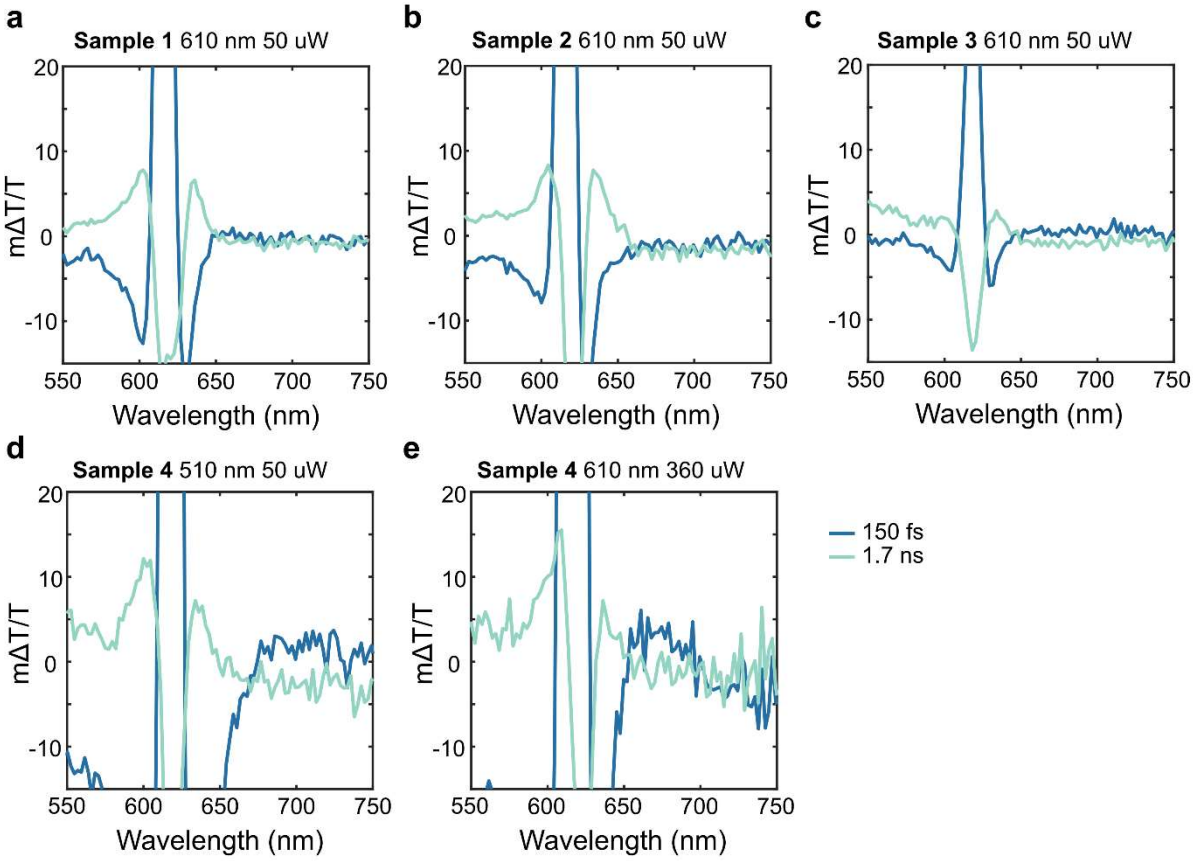

Supplementary Fig. 11 Pump-probe spectra of four untreated monolayer WS_2 samples (Sample 1 is used in the main text). Transient absorption spectra at short (150 fs) and long (1.7 ns) time delays of 4 different samples excited at 610 nm (**a**, **b**, **c**, **e**) and 510 nm (**d**) with an excitation power of 50 W (**a**-**d**) and 360 W (**e**).

The single value decomposition

The single value decomposition was performed using Matlab's built-in single value decomposition function [U,S,V] = svd ().

Where U is the left-singular vectors, S is a matrix containing the singular values on the diagonal, and V is the right-singular vectors.

The spectral components (P) were obtained by multiplying the left-singular vectors (U) with the square root of the singular values:

P=U*S.^.5

Similarly, the temporal evolution (T) is obtained by multiplying the square root of the singular values with the transpose of the right-singular vectors (V).

T=Ssvd.^.5*V'

By sorting the singular values in S and plotting them one can analyze the significance of each component's contribution to the total dataset. It can be seen in Figures S2a and S3a that two singular values are significantly larger than the rest for the untreated samples, whereas for the treated sample only one singular value is significantly larger. Similarly, for the untreated samples Figures S10b, c and S11b,c show that two spectral and two temporal components are above the noise level, in line with the two large singular values that were observed. For the treated sample on the other hand, in Figure S11, only one large singular value is observed and there is also only one significant spectral and temporal component above the noise level.

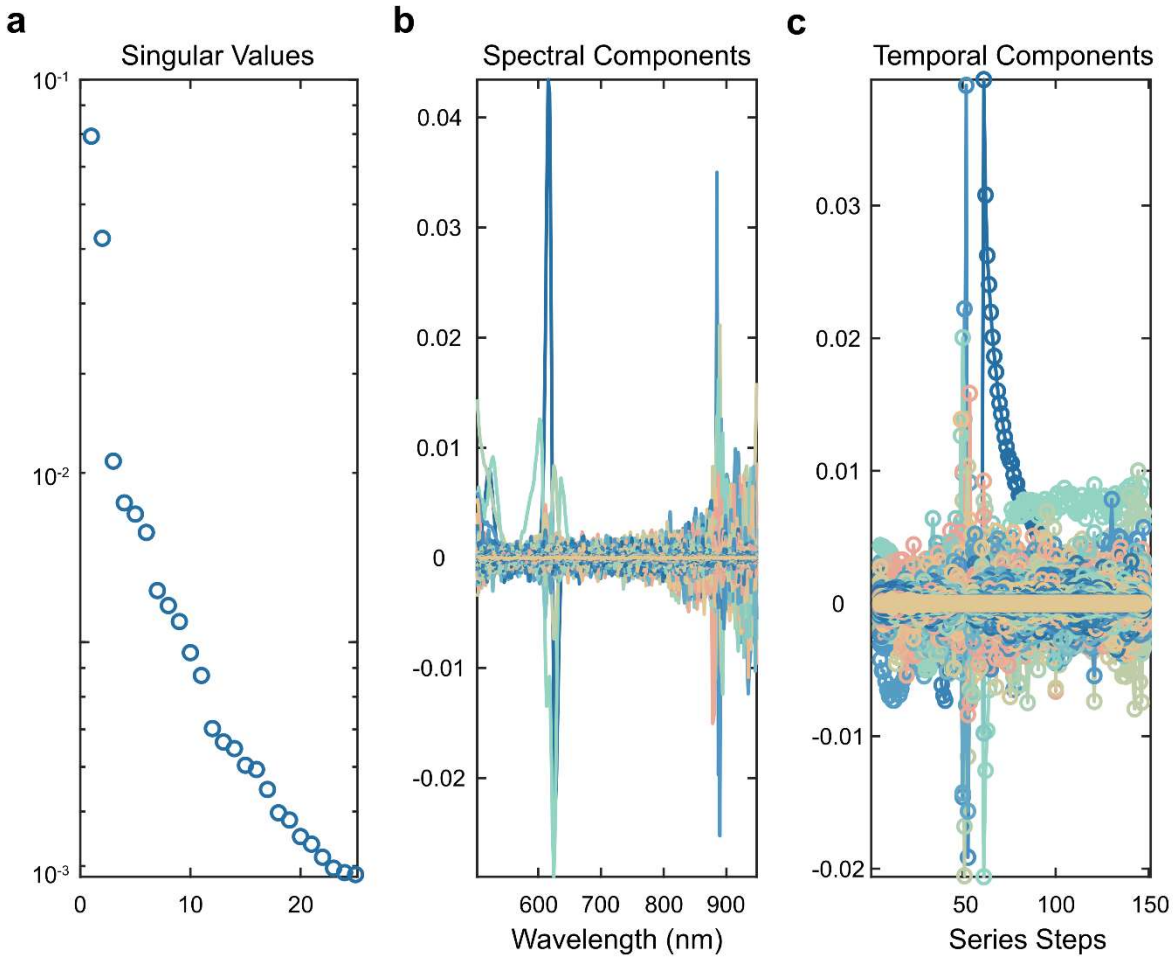

Supplementary Fig. 12 Single value decomposition of transient absorption data for sample 1 untreated. **a** Singular value for the components. **b** Spectral components. **c** temporal profiles extracted by SVD. Two components have significantly larger singular values as well as spectral and temporal features above the noise level (blue and green spectra).

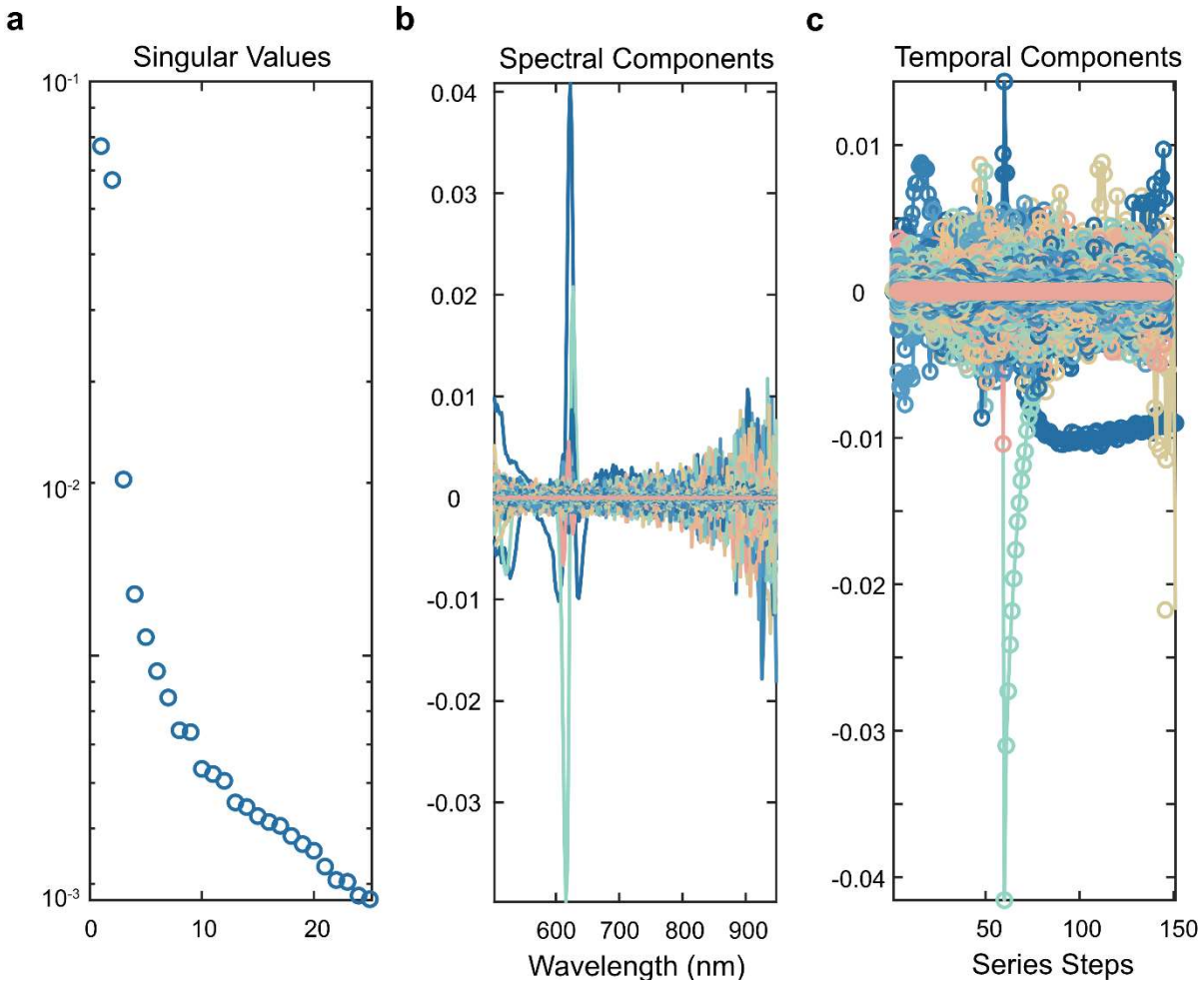

Supplementary Fig. 13 Single value decomposition of transient absorption data for sample 2 untreated. **a** Singular value for the components. **b** Spectral components. **c** temporal profiles extracted by SVD. Two components have significantly larger singular values as well as spectral and temporal features above the noise level (blue and green spectra).

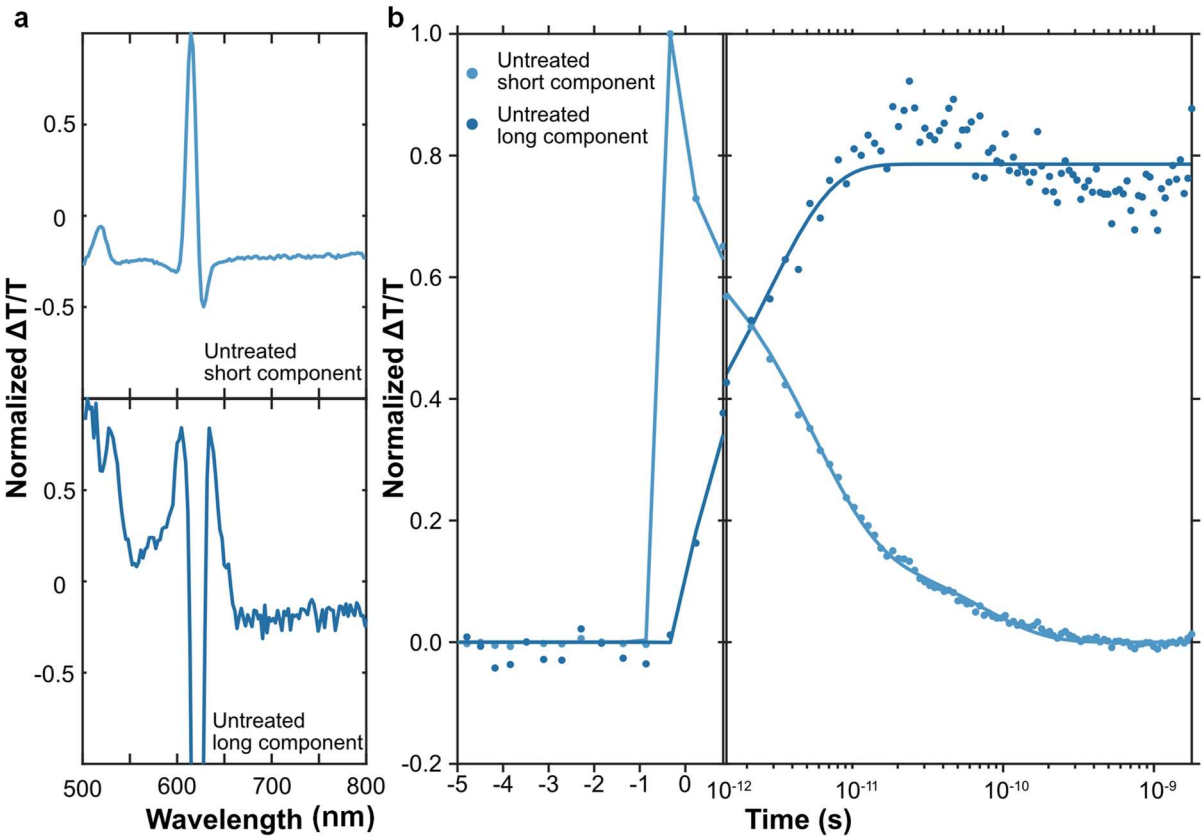

Supplementary Fig. 14 Pump-probe spectra of untreated monolayer WS_2 sample 2. **a** Normalized pump-probe spectra at 150 fs and 1.7 ns. **b** Kinetic profiles for the corresponding spectra in **a** and multi-exponential fits using a 185-fs-wide gaussian response function. The fitting is presented in solid lines.

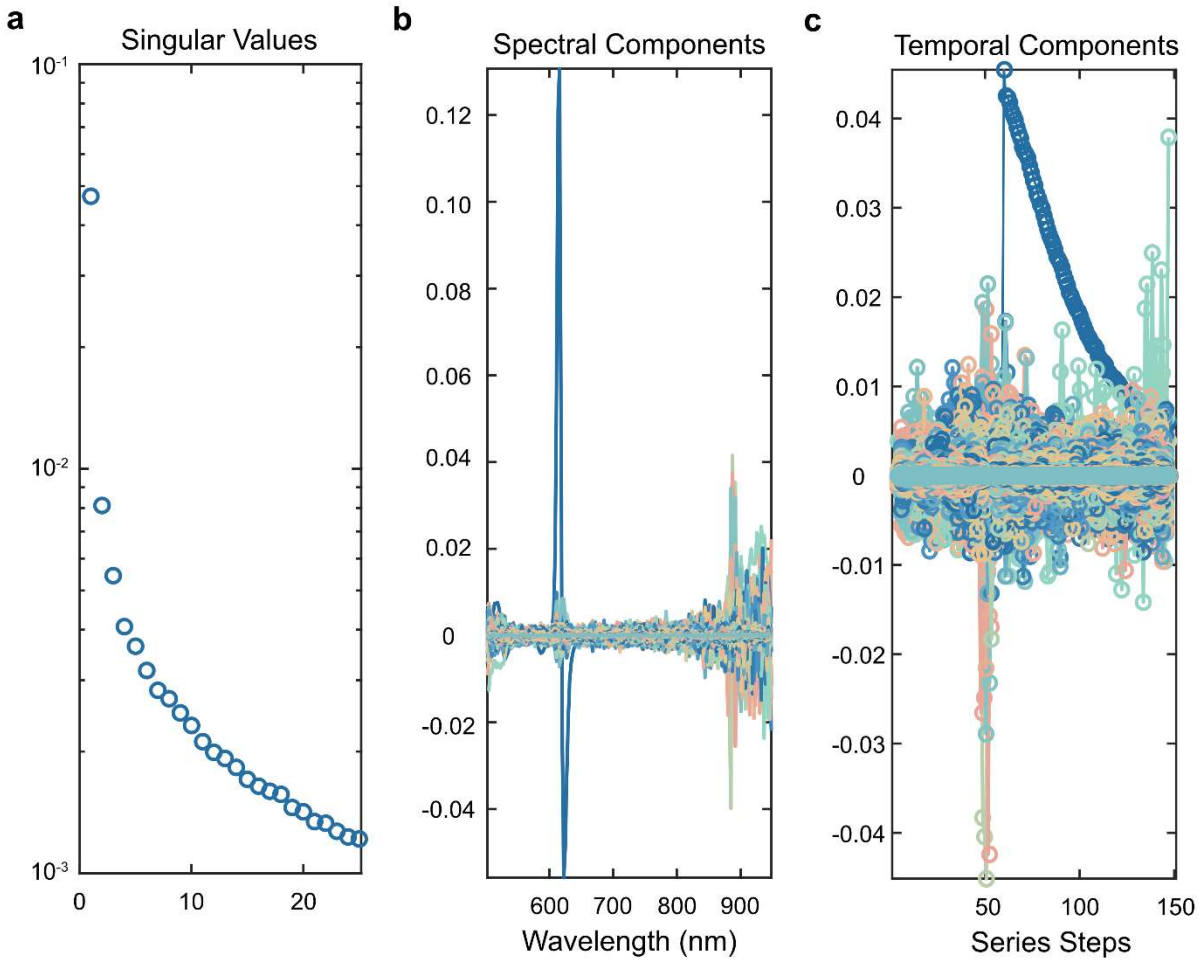

Supplementary Fig. 15 Single value decomposition of transient absorption data for sample 1 treated. **a** Singular values for the components. Spectral components (**b**) and temporal profiles (**c**) extracted by SVD. There is only 1 component with a significantly larger singular value as well as only one spectral and temporal feature above the noise level (blue spectra).

Extracting kinetic profiles for the identified species

From our SVD analysis, we conclude there are two excited state species in the untreated samples and one excited state species in the treated samples. We assign spectra to each species in the following way: For the initially excited species in the untreated samples, as well as the main species in the treated sample the average of the recorded spectra between 100-600 fs is used. For the second species in the untreated samples, the spectra between 0.8-1.8 ns are averaged. The kinetic profile associated with each spectral feature is then obtained in a least-square manner. For example, for the untreated samples, the two spectra were combined as columns in a matrix **A**, where each row contains the intensity value at a corresponding wavelength, and the columns correspond to the first and second species, respectively. The

kinetic profile associated with each spectra (K) is then obtained by taking the pseudoinverse of matrix **A** times a matrix **D** containing all the experimental TA data. The calculations were carried out in MATLAB® using the pinv function:

K = pinv(A)*D

Similarly, the kinetic profile for the single component in the treated sample was extracted in the same way, but with matrix **A** only containing one spectrum.

Fitting of the Kinetic Profiles

The obtained kinetic traces were fit with multi-exponential decays using a deconvolution fitting procedure to account for the Gaussian response function at early times. The multiexponential fitting function can be described by the following equation:

$$I(t) = \sum_i A_i 0.5\, \mathrm{e}^{0.5\left(\frac{\sigma}{\tau_i}\right)^2} e^{-\frac{t-t_0}{\tau_i}} erfc\left(\frac{1}{\sqrt{2}}\left(\frac{\sigma}{\tau_i}\right) - \frac{t-t_0}{\sigma}\right) \quad \text{(S1)}$$

Where σ is the full-width at half max (FWHM) of the Gaussian response function, t_0 is the center of the Gaussian response function τ_i is the lifetime of the *i*th decay and A_i is the pre-exponential factor for the *i*th decay. Fitting was done using a home written MATLAB® script where the experimentally obtained kinetic profile was compared to the analytically described function in Equation S1 where the lifetimes were optimized to minimize the difference using the fminsearchbnd function developed by John D'Errico (2023), MATLAB Central File Exchange.[10] The pre-exponential factors were obtained through linear regression as part of the minimization procedure. The obtained fitting parameters are summarized in Table S1 below.

Supplementary Table 3. Fitting parameters obtained from the fitting of the kinetic profiles.

Parameter	Treated	Untreated Sample 1 First component	Untreated Sample 1 Second component	Untreated Sample 2 First component	Untreated Sample 2 Second component
σ	185 fs	185 fs	185 fs	185 fs	185 fs
t_0	-275 fs	-275 fs	-275 fs	-275 fs	-275 fs
τ_1	15 fs	89 fs	15 fs	46 fs	820 fs
A_1	22.3	5.3	-1.2	8.6	-0.44

τ_2	20.5 ps	7.0 ps	2.6 ps	5.3 ps	6.0 ps
A_2	0.34	0.51	-0.9	0.58	-0.53
τ_3	128 ps	133 ps	17.9 ps	71.0 ps	91 ps
A_3	0.37	0.18	0.16	0.16	0.16
τ_4	3.2 ns	-	300 ns (fixed)	-	300 ns (fixed)
A_4	0.21	-	0.76	-	0.75
$\tau_{average}$	31.5 ps	4.7 ps	-	1.6 ps	-

7. Supplementary Note 7 – Photoelectron spectroscopy data

For the treated sample and the sample treated only with Li-TFSI, the S/W ratio could not be determined as the feature originating from WS_2 was not detected in the S2*p* spectra (Fig. 4). It should be noted that the feature at binding energies around 168 eV originates from the Li-TFSI salt and not from the underlying WS_2 monolayer.[15,16]

As shown in Fig. 4a, the W4*f* core level spectrum of the untreated WS_2 is dominated by a peak with binding energy 32.5 eV, close to reference values of monolayer WS_2.[17–19] This feature is found at similar binding energies in the three treated samples, but the relative intensity of this feature differs between the different surface treatments. After FSH treatment, the relative intensity of the WS_2 feature increases slightly (from 91.2% to 92.3%). The opposite is found for the Li-TFSI and FSH + Li-TFSI treated samples, where this feature makes up only 42.1% and 24.3% respectively. This suggests that there is a strong interaction between the W and Li-TFSI. The peak at higher binding energies, found at 34.8 eV for the untreated sample, corresponds to oxygen bonds and is found in all samples to different degrees.[20] The W5*p* core level is visible at 38.2 eV for the untreated sample. Due to the ionization cross section, this peak is relatively larger than W4*f* in HAXPES spectra compared to XPS spectra. This contrast change is a cross section effect where p-orbitals cross sections decrease slower with increasing photon energy compared to f-orbitals.[21] An addition of metallic tungsten is found in both the Li-TFSI and FSH + Li-TFSI treated sample, at relatively higher levels in the former.[18] Formation of metallic tungsten has previously been accounted for damages to the WS_2

monolayer. This peak is not distinguishable in the HAXPES measurement of the Li-TFSI treated sample, suggesting this effect occur mainly on the immediate surface as the XPS measurements are more surface sensitive. The information depth of spectroscopic measurements increases with a factor of approximately 5 when the photon energy increases from 1486.6 eV (XPS) to 9252.8 eV (HAXPES).[22,23]

As shown in Fig. 4b, the second feature in the S2*p* spectra for these samples presents larger differences in binding energy, specifically at 169.1 eV ($2p_{3/2}$ component) for the Li-TFSI only treated sample and at 169.6 eV ($2p_{3/2}$ component) for the FSH + Li-TFSI treated samples. No signal from the underlying WS_2 is detected in the sulfur 2*p* spectra of these two samples when using the Al-Kα source in XPS measurements. However, in the S1*s* HAXPES spectrum of the Li-TFSI treated sample (Fig. 4c), spectral features from both the Li-TFSI and the WS_2 substrate are identified. This suggests that with a larger photon energy in the HAXPES measurement, information from beneath the Li-TFSI layer can be obtained due to the increased information depth.[22,23] The S1*s* peak originating from the WS_2 layer (2470.1 eV) is consistent across the untreated WS_2, the FSH treated, and the Li-TFSI only treated sample. This consistency implies that the sulfur in the WS_2 layer remains relatively stable following both FSH and Li-TFSI surface treatments, supporting our hypothesis. However, to confirm this stability, a comparison of the sulfur intensity between the samples would be necessary, which is not reliable due to the excess Li-TFSI on the surface from the treatment.

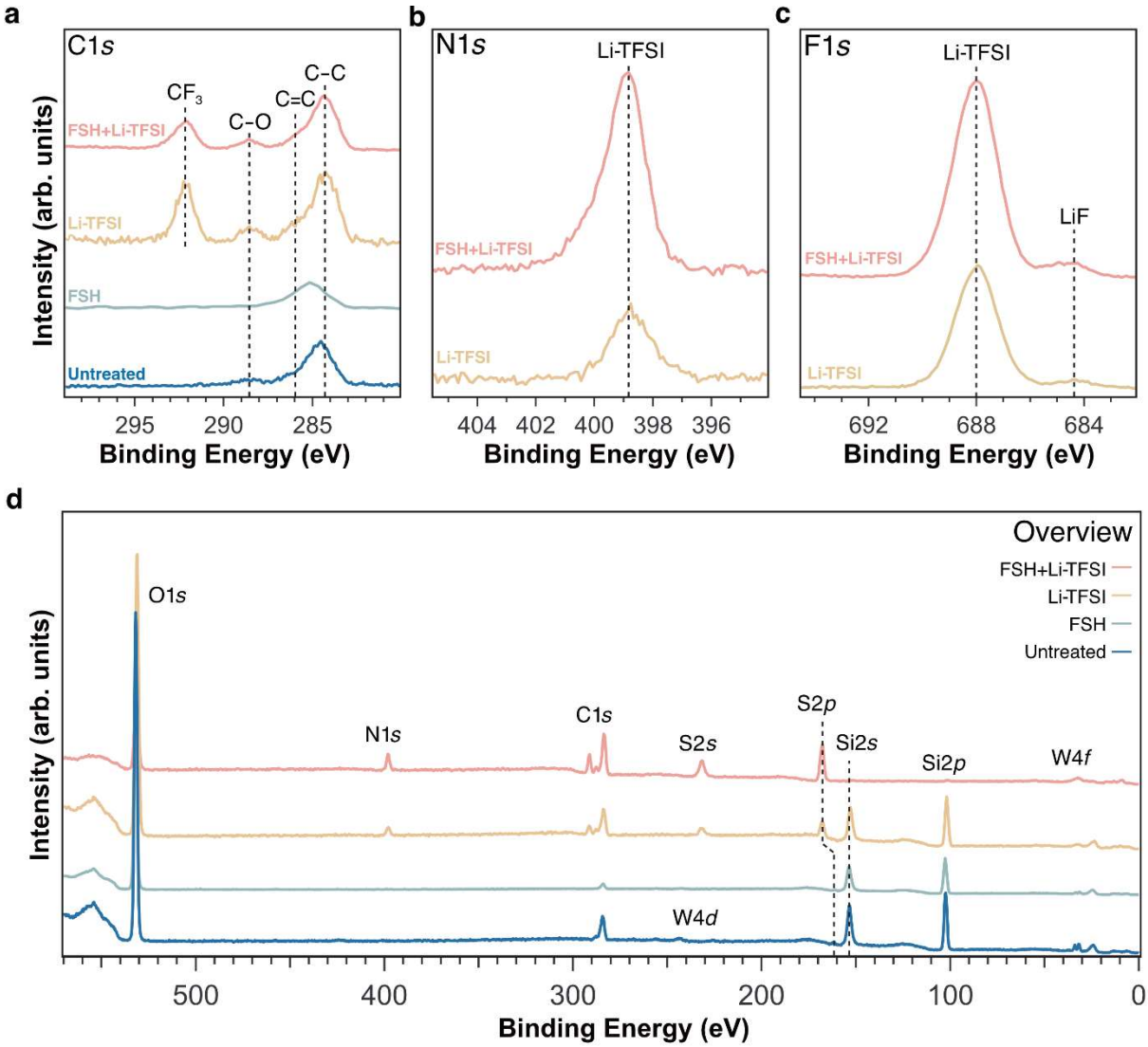

Supplementary Fig. 16 X-ray Photoelectron Spectroscopy (XPS) measurements. Core level XPS spectra in the **a** C1s, **b** N1s and **c** F1s region acquired with photon energy 1486.6 eV. **d** Overview spectra of WS_2, before and after surface treatments.

As shown in Fig. S20 carbon spectra consist of a main peak at lower binding energy that is assigned to carbon contamination (C–C/C=C) on the surface. The Li-TFSI salt contributes with a core level peak at higher binding energies (at 292 eV) seen in both the spectra for Li-TFSI and FSH + Li-TFSI, corresponding to CF_3 bonds in the salt.[15,16] It also adds to the intensity of oxygenated carbon found at 288.5 eV. Both nitrogen spectra display one main peak from the Li-TFSI salt at the same value of 398.8 eV. In the sample treated with FSH and Li-TFSI, another peak emerges as binding energy 400.1 eV which could be attributed to oxygen bonds. In the F1*s* spectra, the main corresponding to Li-TFSI is found at 688.0 eV for both samples. The smaller peak at lower binding energies is assigned to LiF and shows a small shift between

the two samples.[15,24] In the Li-TFSI treated sample, this is at 684.3 eV and for the FSH + Li-TFSI treated sample it is at 684.6 eV. Both nitrogen and fluoride are found only in the Li-TFSI salt, not in the FSH salt, and the slight changes in binding energy in the N1*s* and F1*s* spectra between the two samples originate from the difference of surface below (untreated WS_2 in one case and FSH treated WS_2 in the other case).

Supplementary Table 4. Core level binding energies (eV) for WS_2 before and after surface treatment.

Core level	**Untreated**		**FSH**		**Li-TFSI**		**FSH + Li-TFSI**	
W4*f* XPS	**B.E. (eV)**	**%**	**B.E. (eV)**	**%**	**B.E. (eV)**	**%**	**B.E. (eV)**	**%**
W metal ($4f_{7/2}$, $4f_{5/2}$)					31.4, 33.5	17.7	31.5, 33.6	29.8
WS_2 ($4f_{7/2}$, $4f_{5/2}$)	32.5, 34.6	91.2	32.4, 34.5	92.3	32.2, 34.3	42.1	32.2, 34.3	24.3
WS_3 ($4f_{7/2}$, $4f_{5/2}$)					32.7, 34.8	31.5	32.7, 34.8	27.9
W – O ($4f_{7/2}$, $4f_{5/2}$)	34.8, 36.9	2.1	34.9, 37.0	1.3	33.7, 35.8	6.6	33.7, 35.8	16.0
WS_2 ($5p_{3/2}$)	38.2	6.7	38.2	6.4	38.2	2.1	38.5	2.0
W4*f* HAXPES	**B.E. (eV)**	**%**	**B.E. (eV)**	**%**	**B.E. (eV)**	**%**	**B.E. (eV)**	**%**
W metallic							31.4, 33.5	38.0
WS_2 ($4f_{7/2}$, $4f_{5/2}$)	32.5, 34.6	36.2	32.4, 34.5	35.9	32.2, 34.3	22.3	32.1, 33.2	25.4
WS_3 ($4f_{7/2}$, $4f_{5/2}$)					32.7, 34.8	15.2	33.1, 35.2	28.7
W – O ($4f_{7/2}$, $4f_{5/2}$)	35.9, 38.0	4.3	35.6, 37.7	2.4	35.5, 37.6	3.8	34.1, 36.2	7.2
WS_2 ($5p_{3/2}$)	38.1	59.5	37.7	61.7	38.0	58.7	38.5	0.8
S2*p*	**B.E. (eV)**		**B.E. (eV)**		**B.E. (eV)**		**B.E. (eV)**	
WS_2 ($2p_{3/2}$, $2p_{1/2}$)	162.0, 163.1		162.0, 163.1					

Li-TFSI			168.4, 169.5 169.1, 170.2	168.3, 169.4 169.6, 170.7
S1*s*	**B.E. (eV)**	**B.E. (eV)**	**B.E. (eV)**	**B.E. (eV)**
WS_2	2470.1	2470.2	2470.2	
Li-TFSI			2477.5	2478.0

Core level	**Untreated**	**FSH**	**Li-TFSI**	**FSH + Li-TFSI**
C1*s*	**B.E. (eV)**	**B.E. (eV)**	**B.E. (eV)**	**B.E. (eV)**
C – C	284.6	285.1	284.2	284.3
C = C	286.1		285.8	285.7
C – O	288.6		288.5	288.6
Li-TFSI (CF_3)			292.2	292.1
N1*s*			**B.E. (eV)**	**B.E. (eV)**
Li-TFSI			398.8	398.8
Li-TFSI				400.1
F1*s*			**B.E. (eV)**	**B.E. (eV)**
LiF			684.3	684.6
Li-TFSI			688.0	688.0

8. Supplementary Note 8 – DFT data

Adsorption of FSH vs. Methanol

Since methanol has been used as a solvent in the chemical treatment protocol, the starting point here is to check whether methanol would influence the passivation of these defects or coverage of the WS_2 monolayers. Calculations of adsorption energies of methanol *vs.* 2-furanmethanothiol (FSH) molecule considered a defect-free 2D surface, 2D surface with a neutral sulfur vacancy (SV) defect, and a negatively charged sulfur vacancy defect, since these two are the most common SV types in 2D WS_2 layers.[11] The results have shown that the adsorption of FSH molecule ends with a negative adsorption energy (exothermic reaction as has been defined) only on the non-defective WS_2 layer while methanol does not adsorb on the layers in any considered case (Table S5). The stronger probability of finding FSH on the non-defective surface of the layers is a result of the wan-der-walls interaction between this molecule

and the 2D WS_2 layer. This probability is much lower for the case of methanol. Though it is likely that thiol physisorbs and cover the 2D layer, such weak interaction does not change the electronic structure of the layer as shown in Figure S17 and S18, which cannot explain the observed PL enhancement after the chemical treatment.

Supplementary Table 5. Chemisorption and physisorption investigated to highlight the effects of each adsorbate on the 2D WS_2 layers and defective 2D WS_2 layers.

Chemisorption/physisorption cases	**Adsorption energy (eV)**
Physisorption of methanol on the 2D WS_2 surface	0.60
Physisorption of methanol on the neutral SV defect	0.80
Physisorption of methanol on the SV charged defect	0.73
Physisorption of FSH on the WS_2 surface	-0.03
Physisorption of FSH on the neutral SV defect	0.03
Physisorption of FSH on the SV charged defect	0.56
Chemisorbed thiol (-S-H bond break) on the neutral defect with left H forming H_2	-0.75
Chemisorbed thiol (-S-H bond break) on the charged defect with left H forming H_2	-0.01
Chemisorbed thiol (-S-H bond break) on the neutral defect with left H going to WS_2 surface	1.13
Chemisorbed thiol (-S-H bond break) on the charged defect with left H going to WS_2 surface	1.25
Chemisorbed thiol (-S-H bond break) on the neutral defect with left H goes to a second defective case	-1.12
Chemisorbed thiol (-S-H bond break) on the charged defect with left H goes to a second defective case	-0.67

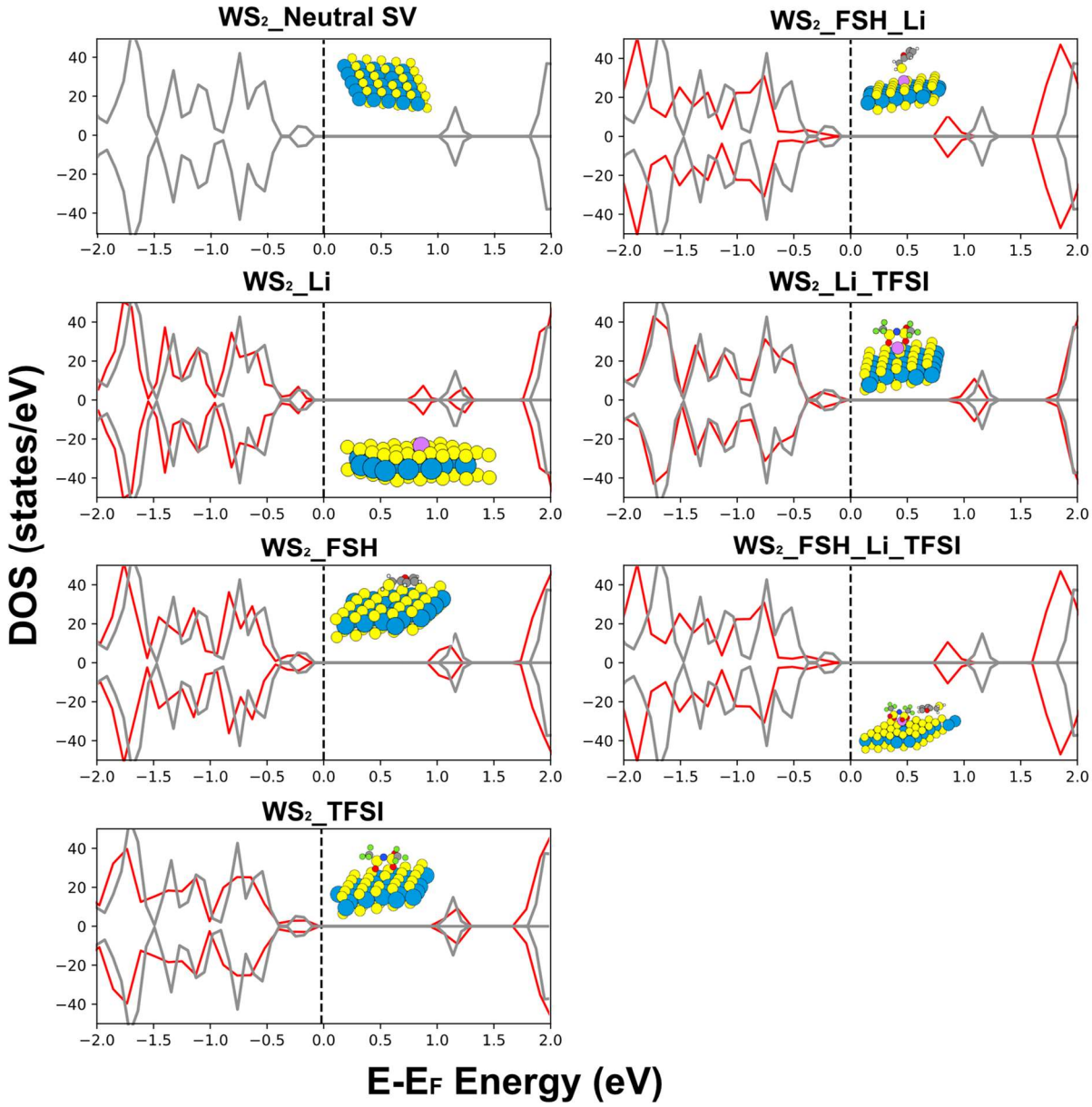

Supplementary Fig. 17 Summed PDOS on the WS_2 layer atoms for the system without adsorbates (grey) and with adsorbates (red). Here, a neutral SV defect is considered.

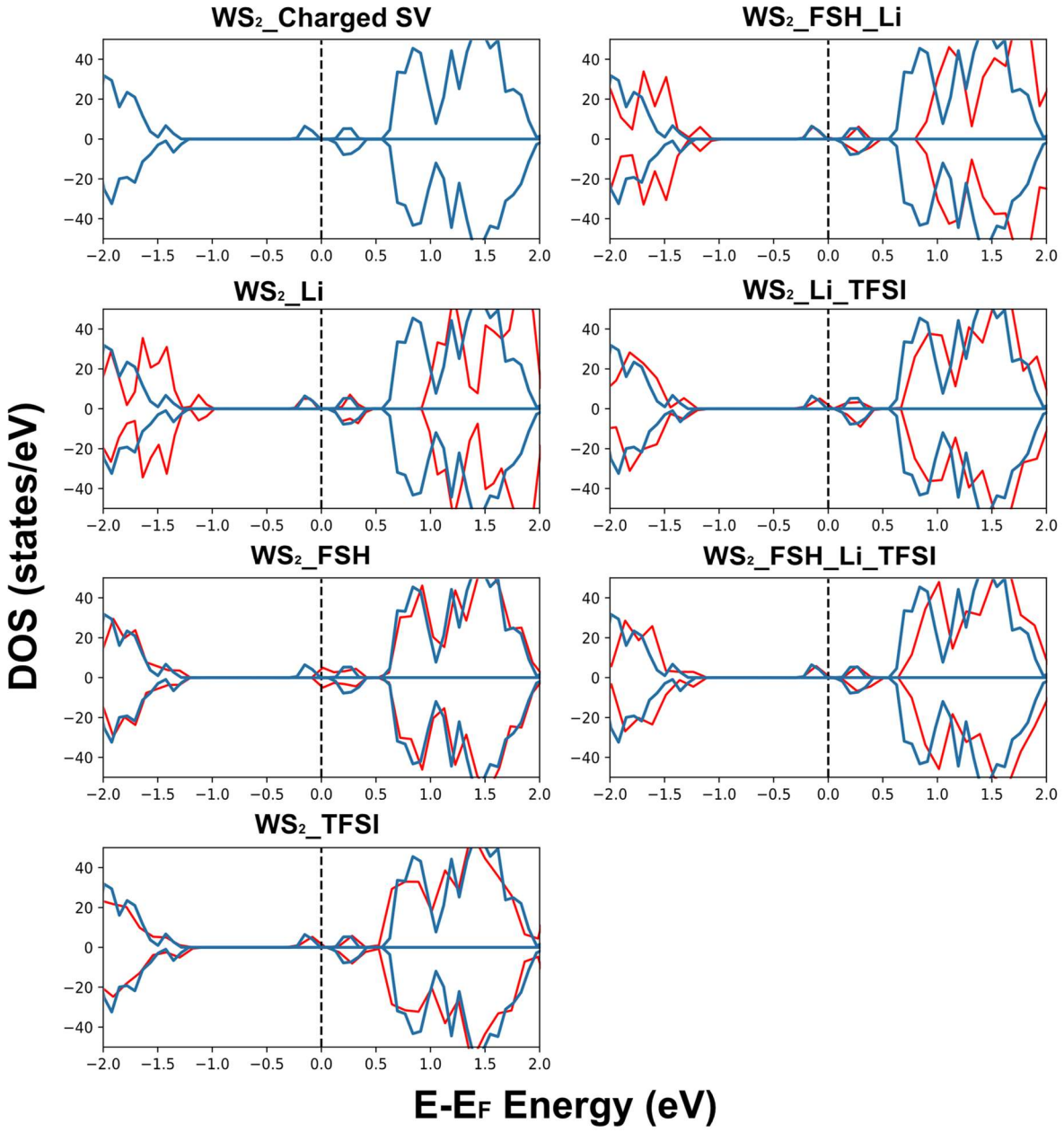

Supplementary Fig. 18 Summed PDOS on the WS_2 layer atoms for the system without adsorbates (blue) and with adsorbates (red). Here, a charged SV defect is considered.

Chemical Adsorption of FSH

The bond cleavage between S and H producing a covalent bond between -S and the SV defective WS_2 monolayer is a possibility that would directly affect the electronic structure of the WS_2 2D layer. This possibility is investigated considering three possibilities: i) The protons from the -SH group in the FSH molecule combine and form H_2 after the cleavage; ii) The protons from the -SH group in the FSH molecule get adsorbed on the surface of the 2D layer

after the cleavage; and iii) The protons from the -SH group in the FSH molecule get adsorbed on another SV defect on the surface of 2D WS_2 layer. These possibilities are evaluated considering two types of 2D WS_2 layer: 2D WS_2 layer with the neutral SV defects and 2D WS_2 layer with negatively charged SV defects. Clearly, the cleaved -S molecule prefers to adsorb on the neutral SV defect as compared with the negatively charged SV (see Table S5). Moreover, depending on where the lost proton adsorbs, the bond cleaved between S and H becomes thermodynamically likely. For the first scenario, where H_2 is formed, an adsorption energy of –0.75 eV is computed (Figure 5a). By bonding the thiol on the neutral SV defect and adsorbing the proton on a second sulfur defect, an adsorption energy of the order of –1.12 eV is computed (Figure S19). Both scenarios involve exothermic reactions. On the other hand, it is unlikely that the lost proton gets adsorbed on the 2D surface according to our DFT simulation that yielded positive adsorption energies of 1.13 eV and 1.25 eV for the neutral and charged defects, respectively. From this analysis, one can infer that the bond cleavage of the thiol group would more likely lead to the formation of a newer bond between the -S molecule and the neutral SV defect with a minor chance to bond on the SV charged defect, but still the thermodynamic driving force for the -S-H cleavage depends on the local environment. Zhang *et al.* have shown via ab initio molecular dynamics (AIMD) that thiol deprotonation has a barrier of only 0.17 eV for the case of 2D MoS_2.[12] They also showed pH-dependent adsorption energy in agreement with our findings that the local environment can affect the passivation of the SV defects by controlling the chemical potential felt by the left proton. Though the electronic structure of the defective 2D layer does not change with the physiosorbed FSH molecule, the formation of a new chemical bond, on the other hand, displayed an effect on the electronic structure of the 2D layer. As shown in Fig.5a, the localized defective states are split into the band gap and shifted to energies closer to the top of the conduction band with the chemical adsorption of FSH. This turns the defects shallower and less likely to trap electrons.

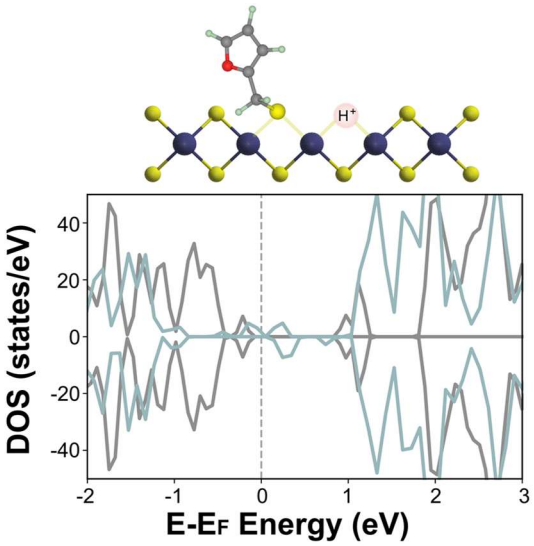

Supplementary Fig. 19 A possible mechanism for how small molecule FSH interact with the WS_2 monolayer surface using DFT calculation.

Adsorption of Li-TFSI

To elucidate the effects associated with the developed chemical treatment protocol, we conducted a comprehensive analysis, commencing with electronic structure calculations (summed PDOS of the atomic layer) for distinct cases (Fig.S17 and S18). Our objective was to identify modifications capable of inducing changes in the layer's electronic structure, subsequently influencing the PL intensities. Subsequently, a thermodynamic analysis was employed to assess the feasibility of scenarios altering the layer's electronic structure. The only case that induced a modification in the summed PDOS of the layer was the adsorption of Li^+. Notably, for the neutral SV defects, this modification occurred exclusively when the FSH coordinates the Li^+.

Since Li^+ is found to be one of the main responsible for inducing changes in the 2D WS_2 electronic structure, we investigate the probabilities if finding these at the defects. Comparative energetics of Li^+ on the SV defect vs. Li^+ adsorbed on the 2D layer surface, with and without FSH coordination (the schematic pictures are shown in Figure S20) demonstrated that the presence of FSH coordinating with Li^+ stabilized the adsorption energy for both the neutral and charged SV defects involved scenarios. For the scenario involving neutral SV defects without the FSH molecule, the energy of the system where Li^+ stands on the surface of the WS_2 instead of on the SV defect is -0.13 eV lower in energy. So, for this case, it is more likely to find Li^+ cations on the WS_2 surface than located at the SV defect. In contrast, when FSH is considered,

the system with Li+ at the SV defect is -0.55 eV lower in energy than the case where Li^+ is at the WS_2 surface. Similarly, for the negatively charged SV defect, the noncoordinating case exhibited a Li^+ energy difference of – 0.44 eV, while coordination with the FSH molecule lowered it to – 0.95 eV. This energetics analysis suggests a higher likelihood of finding Li^+ on SV defective sites when the cations are coordinated by the FSH molecule (Figure 5c).

These phenomena were also predicted by ab initio molecular dynamics (AIMD) simulations using VASP (Video S1 neutral defect and S2 with charged defect). These calculations were carried out with a single-centered k-mesh and a cut-off of 400 eV. A time step of 0.75 fs was employed, resulting in a sample equilibration of 30 ps for further analysis. The temperature was set to 400 K in the canonical ensemble (fixed particle number, volume, and temperature, NVT), and a Nose-Hoover thermostat was used.[13] This slightly higher temperature was chosen to accelerate the dynamic process.

Two significant points emerge: i) In the scenario involving negatively charged defects, the presence of ions drives the electron cloud closer to Li^+, resulting in electron removal from the 2D layer, resulting in a p-doping effect. ii) The presence of the FSH molecule facilitates the stable Li^+ adsorption on defect sites, as evidenced by comparative energy results. We have previously confirmed the positive impact of Li-TFSI on PL intensities, attributing it to the surface p-doping which suppresses the trion formation.[9] Similarly, Zhang *et al.* demonstrated increased PL intensity with p-doping in transition metal dichalcogenides, explained by a reduction in negative carriers and subsequently lower trion formation.[14] Our findings align with these observations, highlighting a similar p-doping effect, yet with enhanced probabilities of finding Li^+ on SV defects due to the FSH coordination.

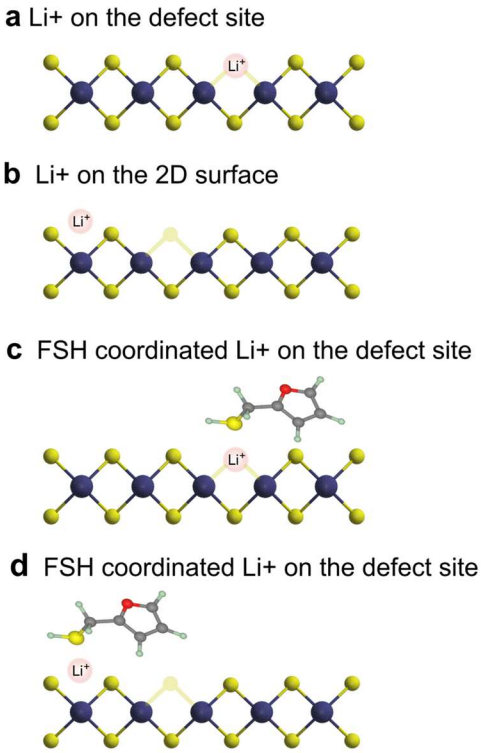

Supplementary Fig. 20 Schematic pictures of the scenarios where **a** Li+ is adsorbed on the SV defect site. **b** Li+ is adsorbed on the 2D layer surface. **c** Li+ is adsorbed on the SV defect site. with the coordination of FSH molecule. **d** Li+ is adsorbed on the 2D layer surface with the coordination of FSH molecule.

9. References

1. Roy, S. & Bermel, P. Electronic and optical properties of ultra-thin 2D tungsten disulfide for photovoltaic applications. *Solar Energy Materials and Solar Cells* **174**, 370–379 (2018).
2. Patanen, M. *et al.* Free atom 4f photoelectron spectra of Au, Pb, and Bi. *Journal of Electron Spectroscopy and Related Phenomena* **183**, 59–63 (2011).
3. Shirley, D. A. High-Resolution X-Ray Photoemission Spectrum of the Valence Bands of Gold. *Phys. Rev. B* **5**, 4709–4714 (1972).
4. Kresse, G. & Furthmüller, J. Efficient iterative schemes for *ab initio* total-energy calculations using a plane-wave basis set. *Phys. Rev. B* **54**, 11169–11186 (1996).

5. Kresse, G. & Joubert, D. From ultrasoft pseudopotentials to the projector augmented-wave method. *Phys. Rev. B* **59**, 1758–1775 (1999).

6. Perdew, J. P., Burke, K. & Ernzerhof, M. Generalized Gradient Approximation Made Simple. *Phys. Rev. Lett.* **77**, 3865–3868 (1996).

7. Grimme, S., Antony, J., Ehrlich, S. & Krieg, H. A consistent and accurate *ab initio* parametrization of density functional dispersion correction (DFT-D) for the 94 elements H-Pu. *The Journal of Chemical Physics* **132**, 154104 (2010).

8. Grimme, S., Ehrlich, S. & Goerigk, L. Effect of the damping function in dispersion corrected density functional theory. *J Comput Chem* **32**, 1456–1465 (2011).

9. Li, Z. *et al.* Mechanistic insight into the chemical treatments of monolayer transition metal disulfides for photoluminescence enhancement. *Nature Communications* **12**, 6044 (2021).

10. John D'Errico. fminsearchbnd, fminsearchcon. (2023).

11. Alaa Akkoush, Yair Litman, & Mariana Rossi. A Hybrid-DFT Study of Intrinsic Point Defects in MX2 (M= Mo, W; X= S, Se) Monolayers. *Physical status solidi a* **221**, 2300180 (2024).

12. Zhang, M. *et al.* Super-resolved Optical Mapping of Reactive Sulfur-Vacancies in Two-Dimensional Transition Metal Dichalcogenides. *ACS Nano* **15**, 7168–7178 (2021).

13. Daan Frenkel & Berend Smit. *Understanding Molecular Simulation From Algorithms to Applications*. (Academic Press, 2002).

14. Zhang, S. *et al.* Controllable, Wide-Ranging n-Doping and p-Doping of Monolayer Group 6 Transition-Metal Disulfides and Diselenides. *Advanced Materials* **30**, (2018).

15. Dedryvère, R. *et al.* XPS Valence Characterization of Lithium Salts as a Tool to Study Electrode/Electrolyte Interfaces of Li-Ion Batteries. *J. Phys. Chem. B* **110**, 12986–12992 (2006).

16. Leroy, S., Martinez, H., Dedryvère, R., Lemordant, D. & Gonbeau, D. Influence of the lithium salt nature over the surface film formation on a graphite electrode in Li-ion batteries: An XPS study. *Applied Surface Science* **253**, 4895–4905 (2007).

17. Villamayor, M. M. S. *et al.* Wafer-sized WS_2 monolayer deposition by sputtering. *Nanoscale* **14**, 6331–6338 (2022).

18. Sundberg, J. *et al.* Understanding the effects of sputter damage in W–S thin films by HAXPES. *Applied Surface Science* **305**, 203–213 (2014).

19. McCreary, K. M., Hanbicki, A. T., Jernigan, G. G., Culbertson, J. C. & Jonker, B. T. Synthesis of Large-Area WS2 monolayers with Exceptional Photoluminescence. *Sci Rep* **6**, 19159 (2016).

20. Scarfiello, R. *et al.* An Insight into Chemistry and Structure of Colloidal 2D-WS2 Nanoflakes: Combined XPS and XRD Study. *Nanomaterials* **11**, 1969 (2021).

21. Rosmej, F. B., Vainshtein, L. A., Astapenko, V. A. & Lisitsa, V. S. Statistical and quantum photoionization cross sections in plasmas: Analytical approaches for any configurations including inner shells. *Matter and Radiation at Extremes* **5**, 064202 (2020).

22. Shinotsuka, H., Tanuma, S. & Powell, C. J. Calculations of electron inelastic mean free paths. XIII. Data for 14 organic compounds and water over the 50 eV to 200 keV range with the relativistic full Penn algorithm. *Surface & Interface Analysis* **54**, 534–560 (2022).

23. Tanuma, S., Powell, C. J. & Penn, D. R. Calculations of electron inelastic mean free paths. IX. Data for 41 elemental solids over the 50 eV to 30 keV range. *Surface & Interface Analysis* **43**, 689–713 (2011).

24. Ismail, I., Noda, A., Nishimoto, A. & Watanabe, M. XPS study of lithium surface after contact with lithium-salt doped polymer electrolytes. *Electrochimica Acta* **46**, 1595–1603 (2001).